Microstructural and metabolic alterations in the zebrafish brain induced by toll-like receptor 2 deficiency: insights from ultra-high field magnetic resonance imaging and spectroscopy

Singer, R.

1

GENERAL INTRODUCTION AND THEORETICAL BACKGROUND

Neurological disorders are the leading cause of diminished health and disabilities worldwide[1]. Approximately 43.1% of the world population, or 3.40 billion individuals, are estimated to have a neurological disorder affecting their central nervous system (CNS); an increase of 58.8% compared with 1990. In addition to the growing number of individual cases, the total disability-adjusted life years (DALYs) of neurological disorders, a method to measure the burden of a disease or condition, increased by 18.2% since 1990[1] (see Figure 1.1). Strokes, neonatal encephalopathy, migraine, dementia, diabetic neuropathy, meningitis, epilepsy, pre-term birth, autism spectrum disorder, and nervous system cancer constitute the top ten major contributors of neurological conditions with the highest DALYs, many of which reported an increase in occurrence since 1990 (see Figure 1.1). Besides significant personal

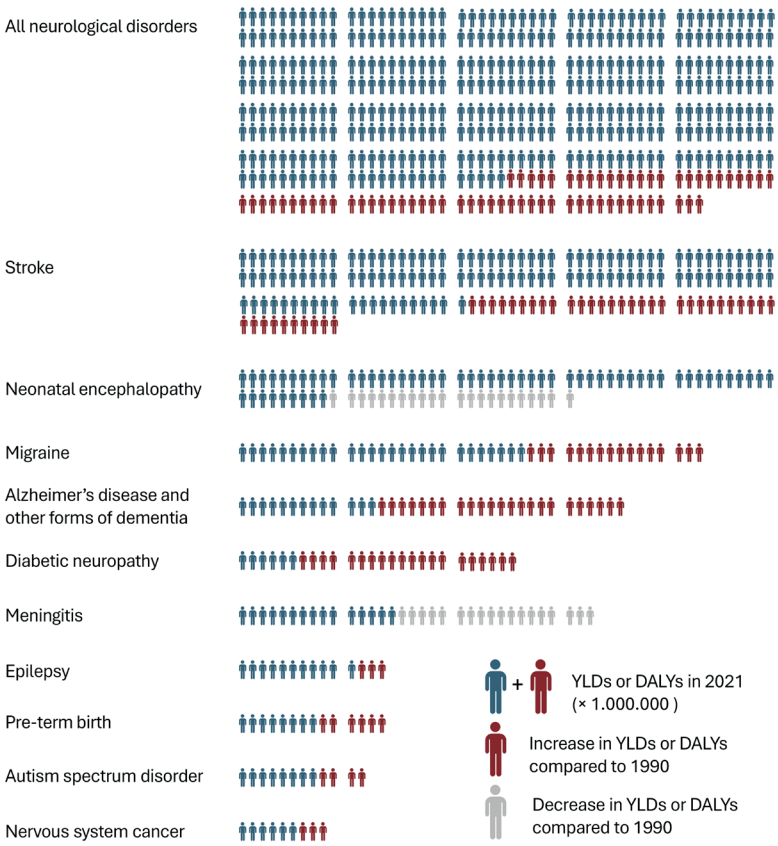

Figure 1.1 *Total number of years lived with disability (YLDs) or disability-adjusted life-years (DALYs) for the top ten neurological disorders from 204 countries and territories in 2021, compared to 1990. Each Figure represents one million (1 000 000) counts. For visualization purposes, numbers have been rounded to the nearest million count. Data obtained from the G. B. D. Nervous System Disorders Collaborators[1].*

impact, neurological disorders impose a substantial economic impact; the annual costs were estimated at approximately 800 billion US dollars in both the United States of America and Europe[2,3]. These numbers are expected to escalate in the coming decades. For instance, the number of people suffering from Alzheimer's disease, the most common form of dementia, is projected to rise from 48 million in 2015 to 131.5 million in 2050, an astonishing increase of 274% in 35 years[4]. The projected growth in the number of patients, combined with rising costs and a current lack of effective treatments for many neurological disorders, underscores the urgent need for scientific research focused on understanding the underlying pathological mechanisms and developing potential therapies.

Animal models of human neurological disorders play a crucial role in many scientific studies[5,6]. These models allow researchers to study the complexities of neurological diseases, facilitating a comprehensive understanding of their development and progression. To a much higher level than possible with human subjects, animal models enable longitudinal studies that track the pathological progression from very early stages, or even before the onset of the disease, providing invaluable insights into the earliest detectable changes. Additionally, animal models offer the unique advantage of controlled experimental conditions, which are often not feasible in human studies. This control allows for precise manipulation of variables and detailed observation of the effects of potential therapies over extended periods. Researchers can systematically explore the efficacy and safety of new treatments, identify potential side effects, and refine therapies with a level of detail and accuracy that is unattainable in human clinical trials. Moreover, animal models allow studying the genetic, molecular, and cellular mechanisms underlying neurological disorders. By replicating specific aspects of human diseases in animals, scientists can investigate the role of genes, proteins, and cellular processes in disease onset and progression. This knowledge is essential for identifying novel therapeutic targets and developing treatments that can more effectively address the root causes of these conditions.

1. NEUROLOGICAL CONDITIONS, THE IMMUNE SYSTEM, AND TOLL-LIKE RECEPTORS

1.1 The immune system

Many neurological disorders are intricately linked to the immune system. Conditions including multiple sclerosis[7], Alzheimer's disease[8], and Parkinson's disease[9] show significant associations with immune system dysregulation. The immune system operates on two primary defence mechanisms: innate immunity and adaptive immunity. The adaptive immunity is a specialised defence mechanism that recognises and targets specific pathogens. Its receptors

are formed through the somatic recombination of gene segments, allowing the immune system to recognise a wide variety of pathogens and mount specific responses against them. This process enables the immune system to adapt to the extensive diversity of antigenic structures and the adaptive capabilities of pathogens to mutate[10]. Despite the versatility of the adaptive immune system, it is slow, potentially requiring weeks to mount a specific response against new pathogens[10]. This timeframe includes the activation and proliferation of antigen-specific T and B lymphocytes, leading to the production of antibodies and memory cells that provide long-term immunity. Conversely, the innate immune system is the body's first line of defence against many pathogens. It encompasses physical barriers such as the skin and immune cells that engulf and eliminate invaders. These immune responses are facilitated by recognition receptors encoded in the germline genome, enabling rapid reactions against a broad spectrum of pathogens. Part of innate immunity relies on specific molecular determinants that initiate immune responses, recognised by pattern recognition receptors (PRRs). PRRs recognise a broad range of pathogen-associated molecular patterns (PAMPs), originating from potential invasive pathogens, including fungi, bacteria, parasites, and viruses[11]. Due to their indispensable roles, many PAMPs exhibit high degrees of conservation and are resistant to mutations that could potentially compromise their functionality[12]. Beyond PAMPs, PRRs recognise danger-associated molecular patterns (DAMPs), endogenous molecular determinants released during processes including infection, inflammation, and cellular stress[13,14]. DAMPs signal danger to the immune system, triggering inflammatory responses and facilitating tissue repair. The PRRs of the innate immunity are categorised in eight groups: toll-like receptors (TLR), C type lectin receptors (CLR), nucleotide-binding oligomerisation domain-like receptors (NLR), retinoic acid-inducible gene-I-like receptors (RLR), opsonic receptors, AIM2-like receptors (ALR), scavenger receptors, and stimulator of interferon genes (STING)[15].

1.2 Toll-like receptors

Of the eight PRR groups, TLRs are the most studied for they are seen as the primary triggers of innate immune responses[15]. Specific TLRs are essential for distinguishing unique PAMPs and DAMPs, playing a crucial role in the immune response. TLRs are type I integral transmembrane proteins consisting of three main regions: the N-terminal domain, the transmembrane domain, and the C-terminal domain. The ligand binding domain at the N-terminus is responsible for the recognition and binding of PAMPs and DAMPs and located in the ectodomain, extending into the extracellular space. This TLR region is crucial for ligand binding and consists of 16 – 28 Leucine-rich repeats (LRRs) with a horseshoe shape, resembling structures formed by parallel β strands[16]. Conventionally, TLRs are categorised based on their cellular location, either on the cell surface or within the intracellular endosomal membrane. The key differences between TLRs located on the cell surface and those within the endosomal membrane are the types of molecular determinants they recognise and their roles in immune signalling. For

humans, TLR1, TLR2, TLR4, TLR5, TLR6, and TLR10 are located on the cell surface recognizing microbial ligands expressed in the cell wall of pathogens. TLR2 forms heterodimers with TLR1, TLR6, and TLR10 and recognises a wide range of microbial ligands, including triacylated lipoproteins, diacylated lipoproteins, and peptidoglycan (PGN)[17]. Furthermore, TLR4 recognises lipopolysaccharide (LPS) and TLR5 recognises the flagella of motile bacteria[12]. Conversely, TLR located on endosomal membranes bind and recognise pathogen-derived nucleic acid motifs present inside the intracellular space[12]. In humans, these concern TLR3, TLR7, TLR8, and TLR9. TLR3 recognises viral double-stranded RNA (dsRNA), TLR7 and TLR8 single-stranded RNA (ssRNA), and TLR9 the nonmethylated 5'-C-phosphate-G-3' motifs in the DNA (CpG DNA) of viruses and bacteria[12]. The transmembrane domains of TLRs are characteristic of

Table 1.1 *Toll-like receptors identified in humans, mice, and zebrafish*[17,22,23]

Human (*Homo sapiens*)	**Mouse (*Mus musculus*)**	**Zebrafish (*Danio rerio*)**
TLR1	TLR1	TLR1
TLR2	TLR2	TLR2
TLR3	TLR3	TLR3
TLR4	TLR4	TLR4al TLR4ba TLR4bb
TLR5	TLR5	TLR5a TLR5b
TLR6	TLR6	
TLR7	TLR7	TLR7
TLR8	TLR8	TLR8 TLR8a TLR8b
TLR9	TLR9	TLR9
TLR10		
	TLR11	
	TLR12	
	TLR13	
		TLR14
		TLR18
		TLR19
		TLR20a TLR20b
		TLR21
		TLR22

single-pass membrane proteins, consisting of a single transmembrane α-helix that connects the N-terminal extracellular domain to the C-terminal intracellular domain. This region is responsible for anchoring the receptor to the membrane[18]. Finally, the toll-interleukin-1 receptor homology (TIR) at the C-terminus extends into the intracellular space. The TIR is composed of approximately 150 amino acids and initiates signalling. Downstream signalling of TLR after activation is, roughly, defined through two pathways. The majority of TLRs in humans, except TLR3, initiate downstream signalling by recruiting myeloid differentiation primary response 88 (MyD88)[12,19]. Subsequently, MyD88 interacts with Interleukin-1 receptor-associated kinase-4 (IRAK-4), interacting with IRAK-1 and IRAK-2[20]. The IRAKs dissociate from MyD88 and interact with tumor necrosis factor (TNF) receptor-associated factor adaptor protein (TRAF6). TRAF6 subsequently generates the formation of an unconjugated free polyubiquitin chain onto itself[21], which leads to the release of nuclear factor-kappa B (NF-κB), regulating a wide range of immune response genes[12,19]. The second pathway, utilized by TLR3 after dsRNA stimulation, involves the TIR domain-containing adaptor-inducing interferon-β (TRIF). This pathway activates interferon regulatory factor 3 (IRF3), leading to the induction of type I interferons[12,19]. Additionally, TLR4 can initiate the TRIF pathway through the TRIF-related adaptor molecule (TRAM), alongside the MyD88 pathway[12,19].

The number of TLRs varies across species; humans (*Homo sapiens*) possess 10 TLRs, mice (*Mus musculus*) have at least 12 TLRs, and zebrafish (*Danio rerio*) have 20 functional TLRs encoded in their genomes[17,22,23] (see Table 1.1). Additionally, the expression patterns of TLRs differ among species. For instance, in zebrafish, TLRs are highly expressed in the skin, indicating that the skin plays a crucial role in the immune system of zebrafish[24].

1.3 Toll like receptors in neurological disorders

Aside from their presence in cells of the innate immune system, TLRs are expressed in different cells in the CNS. For example, human microglia express TLR 1-9, astrocytes express TLR2, TLR3, and TLR9, oligodendrocytes express TLR2 and TLR3, and neurons express TLR3 and TLR7-9[12]. While TLRs play a positive role in the brain by contributing to neurogenesis, cognitive functioning, behaviour, and neuronal growth and morphology (reviewed by Acioglu, Heary, and Elkabes[25]), their involvement is not without complications. TLR-mediated neuroinflammation, for instance, has been linked to the development of various neurological disorders, encompassing both infectious and non-infectious conditions.

Bacterial meningitis is a prime example of an infectious condition where TLR-initiated pathways cause severe neurological damage. During bacterial meningitis, pathogens breach the blood-brain barrier (BBB) and enter the subarachnoid space. In this space, pathogens rapidly replicate because the immune system is not activated until a high density of pathogens is reached[26].

This delay in immune response allows the infection to escalate unchecked. Bacterial meningitis results in severe, life-threatening inflammation within the subarachnoid space. However, the tissue damage associated with this condition is primarily due to an overreaction of the immune system rather than the direct effect of the pathogens themselves[27,28]. In this context, TLRs, specifically TLR2 and TLR4, play a critical role in initiating the biological processes and pathways that lead to immune dysregulation and subsequent neurological damage. These TLR-mediated pathways highlight the dual role of TLRs in both protecting the CNS and contributing to its vulnerability during infections.

TLRs were revealed to potentially play a role in the pathology of non-infectious neurological disorders, including in Alzheimer's disease[29]. Alzheimer's disease is the most prevalent form of dementia, characterised by progressive cognitive decline that interferes with daily functioning. Amyloid beta (Aβ) plaques, composed of misfolded and aggregated Aβ peptides, play a pivotal role in Alzheimer's pathology. These plaques accumulate outside neurons and are implicated as the driving force behind subsequent abnormalities in the brain, triggering events leading to neurodegeneration. Aβ plaques stimulate neuroinflammatory responses, involving microglia and astrocytes, which further exacerbate neuronal damage. It also has been proposed that neuroinflammatory processes are the main event in Alzheimer's disease pathology[29-31]. The exact role TLRs play in Alzheimer's disease pathology is still under debate. Increased expression of TLR1, TLR2, TLR4, and TLR6 was found in human Alzheimer's disease patients and in Alzheimer's disease animal models or animal models with increased Aβ[32-39]. In the case of TLR9, research reports are inconsistent, showing both increased[34,36] and decreased[32] expression levels in Alzheimer's disease. In addition, there is evidence of disrupted TLR signalling pathways in Alzheimer's disease[40]. However, the activation of several TLRs, specifically TLR2 and TLR4, show conflicting effects on the pathology of Alzheimer's disease. In the case of TLR4, activation on the one hand leads to enhanced removal of cellular waste[41], increased Aβ clearance[42], lower memory disfunction, Aβ deposition, and the increased production of neuroprotective factors and anti-inflammatory cytokines[43,44]. Conversely, other reports show that Aβ induced activation of TLR4 promotes the production of pro-inflammatory cytokines, which triggers astrocyte activation and contributes to amyloid-dependent neuronal death[45]. Similarly, activating TLR2 can enhance Aβ clearance[46]. Animal models of Alzheimer's disease deficient in TLR2 exhibit a more rapid decline in memory and cognitive functions compared to a control group[47]. These models also show elevated levels of Aβ and TGF-β[48], greater neuronal death, brain atrophy, learning impairments, and diminished glial activity[49] compared to control groups. However, other studies suggest TLR2 activation may significantly contribute to Alzheimer's disease pathology through TLR2 induced NF-κB signalling leading to excessive Aβ production[50].

Besides Alzheimer's disease, TLRs potentially play an important role in the pathology of other non-infectious neurological disorders, including in Parkinson's disease[51], amyotrophic lateral sclerosis (ALS)[52], and ischemic strokes[53]. Despite evidence suggesting their involvement, the precise mechanisms by which TLRs influence disease progression are not fully understood. This highlights the need for further research to elucidate their functions and therapeutic potential in neurological disorders.

To study the role specific TLRs play in normal functioning and in pathology, many studies utilize TLR-deficient models. These models help in understanding the intricate mechanisms and pathways associated with TLRs. Among these, zebrafish models have become increasingly popular due to their genetic similarities to humans and the ease of genetic manipulation. TLR-deficient zebrafish models offer valuable insights into the physiological and pathological roles of TLRs, providing a robust platform for further research. In this thesis, a TLR2-deficient zebrafish model is utilized to study the role of TLR2 on normal brain function. The TLR2-deficient zebrafish model is the tlr2^{sa19423} mutant, referred to as *tlr2*$^{-/-}$. It has a thymine to adenine point mutation that creates a premature stop codon. This mutation occurs in the sequence coding for the C-terminus of the leucine-rich repeat (LRR) domain. As a result, the protein is truncated and lacks the Toll/IL-1 receptor (TIR) domain[54]. Previously, Hu *et al.* utilized this TLR2-deficient zebrafish model to study the effect of TLR2 on the metabolic profile in zebrafish larvae[15]. Their research demonstrated that the absence of TLR2 significantly altered the metabolic pathways, providing crucial insights into how TLR2 influences metabolic processes[15].

2. ZEBRAFISH IN NEUROLOGICAL BIOMEDICAL RESEARCH

Mammalian models, particularly rodents, are intensively used for studying neurological conditions for their anatomical and physiological similarities to humans. Many mammalian species have genetic sequences highly homologous to human, allowing gene function studies and disease mechanisms relevant to human conditions. For example, mice share approximately 85% of their protein-encoding genomes with humans[55-58]. Despite these advantages, mammalian models often provide limited high-throughput screening capabilities due to their labour-intensive care requirements[59]. This necessitates a large, specialised staff and infrastructure, significantly increasing both research costs and time. Given these challenges, the zebrafish, a tropical fish native to the southern regions of Asia, developed as a popular alternative model organism in biomedical research. Following its first use as a model organism for studying vertebrate neuronal development by George Streisinger in the 1960s, a groundbreaking paper in 1981 introduced genetic techniques for generating homozygous diploid zebrafish clones[60]. However, it wasn't until the late 1990s that the zebrafish gained

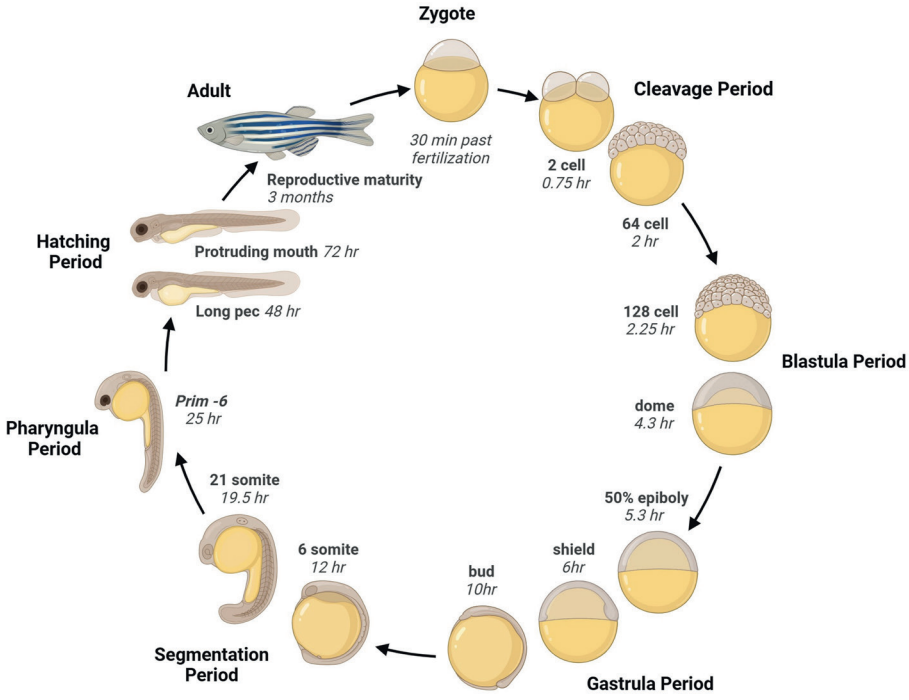

Figure 1.2 *Developmental stages of the zebrafish. After fertilization, the zebrafish embryo develops rapidly, hatching as free-swimming larvae after approximately two days. Next, they reach reproductive maturity after approximately three months. Created with zebrafish developmental timeline template of Biorender.com and printed with permission.*

significant popularity as a model organism in biomedical research, largely due to the pioneering work of Christiane Nüsslein-Volhard (Tübingen, Germany), and Wolfgang Driever and Mark Fishman (Boston, USA)[61].

Compared to other model organisms used in biomedical research, zebrafish offer various advantages to explain their widespread popularity. Female zebrafish reach reproductive maturity within three months and produce approximately 200 to 300 eggs per week. This enables rapid reproduction of transgenic models, facilitating high-throughput experimental screening. In addition, the development of zebrafish embryos and larvae progresses swiftly after *ex vivo* fertilization (see Figure 1.2). Additionally, the transparent nature of zebrafish embryos and larvae allows for internal structures visualization under microscopes. This transparency makes zebrafish exceptionally suitable for monitoring developmental processes. Furthermore, the complete sequencing of the zebrafish genome revealed 84% of genes

associated with human diseases possess corresponding homologous genes in the zebrafish genome. This, coupled with the relative ease of manipulating zebrafish genes, facilitated the creation of numerous mutations in the zebrafish genome, paving the way for the development of many zebrafish models for studying a broad spectrum of pathological conditions.

For biomedical research specifically focussed on neurological disorders, zebrafish gained significant popularity in the last few decades as illustrated in Figure 1.3. Given the obvious anatomical and physiological differences between humans and zebrafish, the organisation of their central nervous systems exhibits remarkable similarities[62]. Various structures in the zebrafish brain exhibit homology with those found in the human brain. For example, the zebrafish telencephalon, situated in the forebrain, consists of the olfactory bulb, pallium, and subpallium. The olfactory bulb is involved in processing of smell related sensory information in both humans and zebrafish, whereas the zebrafish dorsal pallium, medial pallium, lateral pallium, and ventral pallium, are homologues of the human isocortex, amygdala, hippocampus, and piriform cortex, respectively[62]. Furthermore, the zebrafish and human brain alike contain a similar blood brain barrier, protecting the brain from potentially harmful substances while maintaining the brain's internal environment[63]. At the cellular level, the composition of the zebrafish brain closely resembles that of the human brain. Alongside neurons, the zebrafish brain contains similar cells including oligodendrocyte and microglia cells. However, notable differences exist, as zebrafish lack classic stellate astrocytes[64]. Instead, zebrafish fulfil the

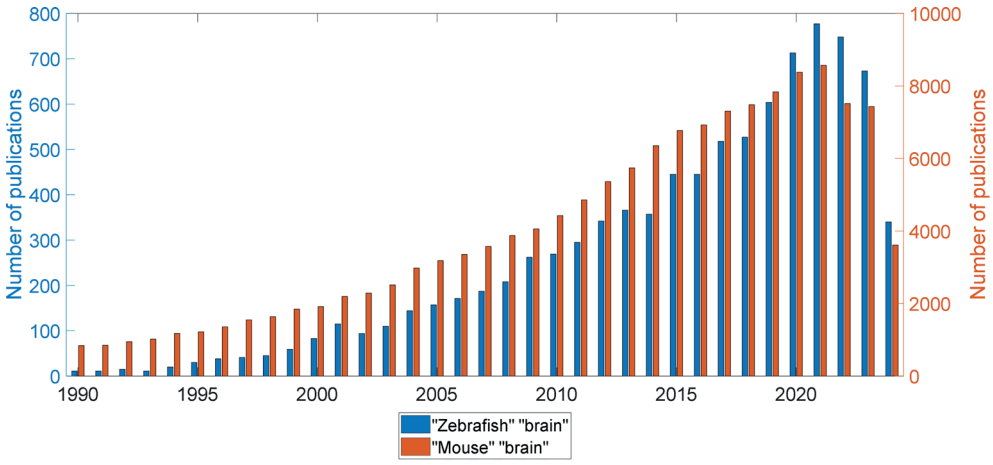

Figure 1.3 *Publication count concerning the zebrafish brain and mouse brain in the pubmed database (National Library of Medicine, National Center for Biotechnology Information, Bethesda, MD, USA). Data acquired by searching for "zebrafish" "brain", and "mouse" "brain", respectively.*

functions typically carried out by mammal astrocytes through radial glial cells[64]. Despite these distinctions, the zebrafish radial glial cells are commonly referred to as astrocytes in literature due to their striking similarities. At the molecular level, the cerebral metabolic profile of zebrafish is remarkably similar to humans and other mammals[65-67], containing identical neurotransmitters, including the main excitatory and inhibitory neurotransmitters glutamate and γ-aminobutyric acid (GABA), respectively. Furthermore, both the zebrafish and human brain contain the same various cell-specific metabolites, including *myo*-inositol (m-Ins) and N-acetylaspartate (NAA), for glial cells and neurons, respectively.

Today, a wide range of transgenic zebrafish models are available for use in biomedical research, covering various neurological disorders. Transgenic models have been developed for neurodevelopmental disorders, including attention deficit hyperactivity disorder (ADHD)[68] and autism spectrum disorders (ASDs)[69]. In the field of neurodegenerative disorders, zebrafish models exist for Alzheimer's disease[70], amyotrophic lateral sclerosis (ALS)[71], Huntington's disease[72], and Parkinson's disease[73]. Additionally, there are models for stroke[74] and cerebrovascular disorders[75], epilepsy and other seizure disorders[76], autoimmune conditions including multiple sclerosis (MS)[77], Schizophrenia[78], traumatic brain injury[79], and brain cancers including glioblastoma[80]. Most biomedical research utilizing zebrafish as a model for neurological conditions focus on several key areas. These include the pathological impact on developmental progression to monitor how neurological disorders manifest and progress over time. Behavioural studies are utilized to monitor behavioural changes associated with neurological disorders, providing insights into the effects of these conditions on motor function, cognition, and social behaviours. Furthermore, transcriptomic studies help identify key genes and molecular pathways involved in the onset and progression of these disorders, while metabolomic studies can identify metabolic changes related to neurological disorders. These studies provide insights into the biochemical pathways and metabolites involved in disease mechanisms, potentially revealing new targets for therapeutic intervention[81]. Finally, for their advantages in comparison to rodents, zebrafish are employed in high-throughput drug screening to identify potential therapeutic compounds and test for toxicity.

3. MAGNETIC RESONANCE IMAGING AND MAGNETIC RESONANCE SPECTROSCOPY

Among the various techniques utilized and discussed in this thesis, magnetic resonance imaging (MRI), diffusion-based MRI (dMRI), and localized magnetic resonance spectroscopy (MRS) stand out as the most important contributors. This section serves as an introduction to the theoretical and technical background of these techniques.

MRI is a well-established non-invasive technique for neurological diagnostics and in biomedical research. Up to date, MRI is the most precise technique for producing highly detailed images of the brain, outperforming other techniques including computed tomography (CT) or Röntgen radiation (X-ray). MRI is a versatile imaging technique capable of creating various types of contrast by exploiting different tissue properties such as proton density, T_1, T_2, diffusion characteristics, or magnetization transfer. This allows for a wide range of contrast options tailored to specific needs. MRI not only differentiates between various cerebral tissue types, including white matter, grey matter, and cerebrospinal fluids, MRI is applied in the diagnostics of a wide range of neurological conditions including brain tumours[82], brain infections[83], brain damage[84], strokes[85], hydrocephalus[86], and intracranial haemorrhage[87]. For many of these conditions, non-invasive diagnostics would not be possible without MRI.

Closely related to NMR, localized MRS is a non-invasive technique to locally provide quantitative biochemical information. However, unlike traditional NMR, localized MRS allows for the selection of a specific region of interest (ROI) through the MRI gradient systems. Hence, the biochemical composition of specific tissue can be monitored in their native biological environment, eliminating the need for laborious extraction procedures. Although MRS is employed for various tissue types[88-91], clinical applications mainly focus on brain tissue and neurological disorders[92-98]. Significant changes in cerebral metabolites have been detected in various neurodegenerative diseases[49,99-111], providing invaluable quantitative biochemical information regarding pathological progression.

In Section 1.3.1, the basics of nuclear magnetic resonance (NMR) are discussed, the foundation upon which MRI, dMRI, and localized MRS are built. Section 1.3.2 treats MRI, covering MRI image construction, generating contrast in MRI, and various MRI pulse sequences utilized in the main work of this thesis. In Section 1.3.3, dMRI is discussed, covering the basic concept of dMRI, diffusion-weighted imaging (DWI), diffusion tensor imaging (DTI), diffusion kurtosis imaging (DKI), and dMRI tractography. Next, in Section 1.3.4, the theoretical background of localized MRS is discussed. Finally, as the main work discussed in this thesis was performed using ultra-high field (UHF) MRI systems, the opportunities and challenges of utilizing these systems is treated in Section 1.3.5.

3.1 Physical basis of nuclear magnetic resonance techniques

MRI and localized MRS are based on the principles of NMR. The NMR phenomenon was first observed in 1946 by two independent research groups; the group of Bloch, Hansen, and Packard[112], and the research group of Purcell, Torrey, and Pound[113], for which Bloch and Purcell received the Nobel Prize for physics in 1952[114]. In this section, the basics of the NMR phenomena are discussed, essential for understanding the foundations upon which this thesis

is constructed. The information provided in this section is mainly provided by "Basic one- and two-dimensional NMR spectroscopy, by Horst Friebolin"[115], unless stated otherwise.

NMR spectroscopy is based upon the interaction between nuclei with a non-zero nuclear spin I and an external magnetic field $\mathbf{B}_0$. Biologically significant chemical elements with NMR detectable isotopes are ^{1}H, ^{13}C, ^{31}P, and ^{15}N, with spin I = ½. Nuclei with I = 0 include ^{12}C and ^{16}O, implying two of the abundant isotopes found in organic compounds cannot be detected through NMR. Isotopes with I > ½ also exist, *e.g.* ^{14}N (I = 1), ^{23}Na (I = 3/2), or ^{43}Ca (I = 7/2). The focus of this thesis is on the abundant I = ½ ^{1}H nuclei.

In a simplified view, nuclear spins may be seen as tiny magnets. In the absence of an external magnetic field, the individual nuclear moments ($\boldsymbol{\mu}_i$) are randomly oriented, and their sum results in no net magnetization **M** (see Figure 1.4). However, in an external static magnetic field $\mathbf{B}_0$, the z-component of the nuclear spin angular momentum $\mathbf{I}_z$ is quantified over $2I + 1$ possible spin states. The spin states are indicated by the magnetic quantum number m, with $m = I, I\text{-}1, \ldots -I$. For nuclear spins with I = ½, the spin states are commonly referred to as α (m = ½, parallel to $\mathbf{B}_0$) and β (m = -½, anti-parallel to $\mathbf{B}_0$). The energy difference ΔE between the spin states α and β is

$$\Delta E = \gamma \cdot \hbar \cdot B_0 \tag{1.1}$$

where γ is the gyromagnetic ratio ($26.7522 \cdot 10^7$ rad T^{-1} s^{-1} for ^{1}H), $\hbar$ is $h/2\pi$, with h being

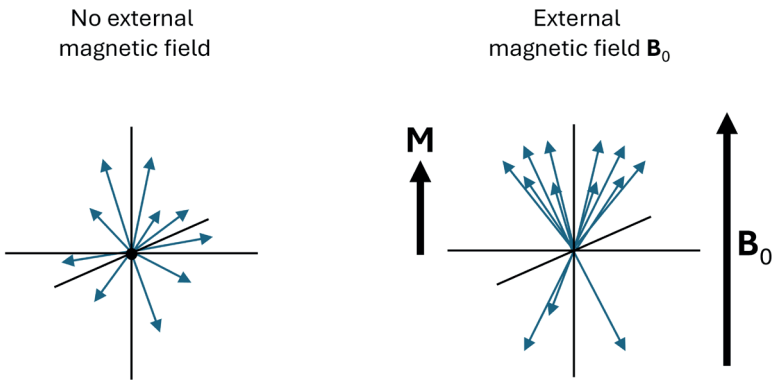

Figure 1.4 *Without an applied magnetic field, spins are randomly oriented, and there is no net nuclear magnetization* ***M****. When an external magnetic field* $\mathbf{B}_0$ *is applied, the z-component of the nuclear spin angular momentum aligns either parallel or antiparallel to* $\mathbf{B}_0$*. Due to a slight preference for parallel alignment over antiparallel alignment, a net magnetization* ***M*** *is generated.*

Table 1.2 *Magnetic field strengths used in NMR and MRI, denoted in Tesla (T) and the Larmor frequency of hydrogen (MHz). *Larmor frequencies were rounded to their conventionally used value.*

Magnetic field strength (T)	Larmor frequency ^{1}H (MHz)*
1.5	64
3	128
7	300
14.1	600
17.6	750
22.3	950
28.2	1200

Planck's constant (6.6256 · 10^{-34} J s), and B_0 is the magnetic field strength in Tesla, with $1\mathrm{T} = 1\left(\frac{\mathrm{N}}{\mathrm{A}\cdot\mathrm{m}}\right)$. The energy difference between the α and β spin states leads to a difference in population due to the Boltzmann distribution, where nuclei occupy the lower-energy α-state more frequently at thermal equilibrium. The nuclear spin state population ratio

$$\frac{N_\beta}{N_\alpha} = e^{\left(\frac{-\Delta E}{k_\mathrm{B}T}\right)} \tag{1.2}$$

is estimated using the Boltzmann distribution. Here, k_B is the Boltzmann constant (1.3805·10^{-23} J K^{-1}) and T is the absolute temperature in K.

The energy difference between the spin states α and β creates a minimal population disparity between β and α states, resulting in a relatively small **M**. Consequently, NMR based techniques have a low sensitivity compared to other analytical techniques. A way of improving the sensitivity of NMR is to increase $\mathbf{B}_0$. Table 1.2 provides an overview of magnetic field strengths (in T and Hz) typically utilized in NMR and MRI systems, as well as in the present study. It is common practice to denote the field strength by referencing the precession frequency of ^{1}H at the corresponding magnetic field strength. The precession frequency, or Larmor frequency ν_L, is given by

$$\nu_\mathrm{L} = \left|\frac{\gamma}{2\pi}\right| B_0 = \frac{\Delta E}{h} \tag{1.3}$$

Hence, a 14.4 T NMR system is also commonly referred to as a 600 MHz system.

3.2 Magnetic resonance imaging

Magnetic resonance imaging (MRI) is a well-established, powerful, non-invasive technique primarily used in the clinical field for imaging soft tissues. Its popularity in clinical settings can be attributed to its relative safety. It does not involve ionizing radiation as used in computed tomography (CT) scans, while offering superior image quality with exceptional detail. MRI can provide remarkable structural details in various soft tissues, including the lungs[116], stomach[117], brain[118], muscles[119], liver[120], breasts[121], kidneys[122], and the heart[123], making it invaluable for monitoring a wide range of pathologies and disorders. Outside the clinical field, MRI is extensively used in research, not only for humans but also for other organisms including rodent models[124], zebrafish models[125], and plants[126]. MRI offers a diverse range of experimental sequences designed for specific imaging needs; from fundamental T_1, and T_2 weighted images, to multi-slice and fast acquisition sequences. Beyond anatomical imaging, MRI extents its utility to advanced applications, including quantification of tissue properties such as T_1 and T_2 relaxation times, assessing diffusion characteristics, specific imaging of lipid signals for estimation of the fat composition, and unravelling neural connectivity patterns through tractography. Central to the diversity of MRI sequences lies the interplay between radio frequency (RF) pulses and the gradient systems utilized for spatial encoding. This chapter serves to introduce fundamental components of MRI sequences and to elucidate the pivotal sequences employed in this thesis.

3.2.1 Spin echo and gradient echo sequences

MRI experiments are generally characterised as spin echo- or gradient echo-based sequences. Basic pulse programs of these sequences are shown in Figure 1.5. While both are widely used in MRI, most experiments in this thesis rely on spin echo sequences. This sub-section will focus on exploring and understanding spin echo-based MRI techniques.

Spin echoes, or Hahn echoes, named after E.L. Hahn who first discovered them in 1950[127], are generated by a sequence of RF pulses. In their most basic form, shown in Figure 1.6, spin echo sequences start with a 90° (1/2 π) RF excitation pulse that rotates the magnetization away from the *z*-axis into the *xy*-plane (Figure 1.6A&B). After the excitation pulse, the spins start to fan out due to loss of coherence from T_2^* and T_2 relaxation processes (Figure 1.6C). Next, a 180° (π) RF refocusing pulse is applied (Figure 1.6D), compensating the local heterogeneities in the magnetic field causing T_2^* relaxation. Consequently, the spins realign, the magnetization is refocused, and an echo of the initial NMR signal is observed at the echo time *TE*, which is in the millisecond range. The 180° refocusing pulse compensates T_2^* relaxation, while the loss of spin coherence caused by pure T_2 relaxation processes develops further during the refocusing period. This feature is utilized in the estimation of T_2 relaxation times of tissue (see Section 1.3.2.4). After the echo signal is recorded, a waiting period is initiated allowing

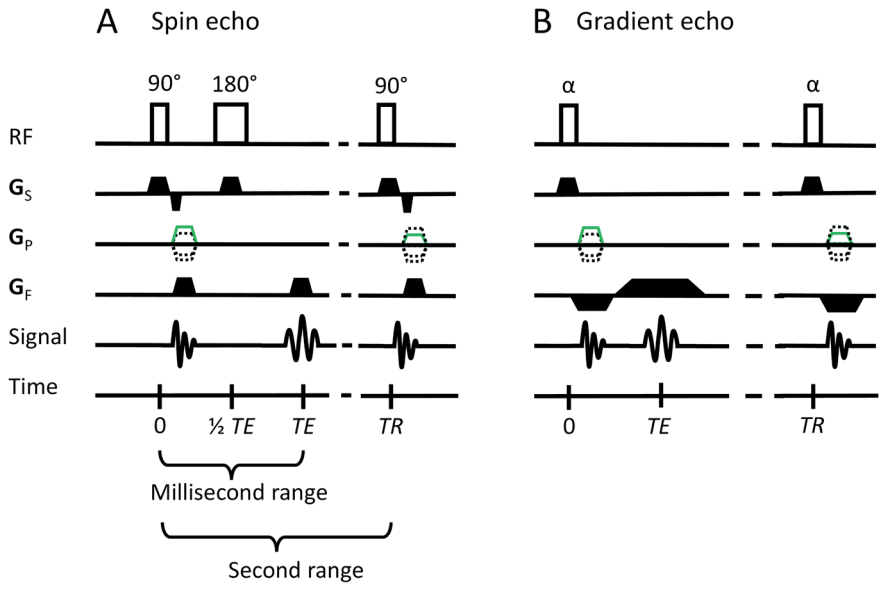

Figure 1.5 Basic [A] spin echo and [B] gradient echo MRI sequences. *Typically, the echo time TE is in the millisecond range, while the repetition time TR is in the second range. However, the precise values depend on the sample, desired contrast, and applied magnetic field strength. Three magnetic gradient systems are utilized for the spatial encoding, namely the slice selection gradient (**G**$_S$), the phase encoding gradient (**G**$_P$), and the frequency encoding gradient (**G**$_F$).*

T_1 and T_2 relaxation processes to complete. A next scan starts with a 90° excitation pulse at repetition time *TR*, which is in the order of seconds. Thus, *TE* << *TR*. The *TE* and *TR* utilized depend on the sample, desired contrast, and $\mathbf{B}_0$.

3.2.2 The rapid acquisition with relaxation enhancement (RARE) sequence

As previously stated, basic spin echo MRI experiments record one phase encoding gradient line per excitation cycle, making the number of phase encoding lines a significant factor in the total measurement time. However, since *TE* << *TR*, with *TE* being in the millisecond range and *TR* in the second range, there is a time interval between *TE* and *TR*. During this interval, T_1 and T_2 relaxation processes are progressing. The rapid acquisition with relaxation enhancement (RARE) sequence utilizes this time interval by implementation of additional 180° refocussing pulses to acquire multiple phase encoding gradient lines per excitation cycle[128]. The total number of 180° refocussing pulses utilized is referred to as the echo train length (ETL), or RARE factor. The MRI sequence of RARE is shown in Figure 1.7.

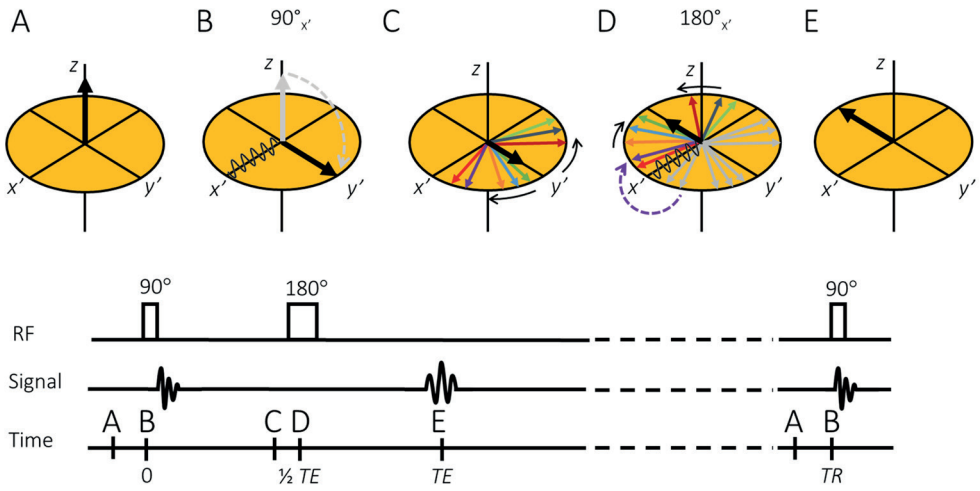

Figure 1.6 Spin echo sequence, illustrating the origin of the echo signal at TE. [A] Initial state. *The system starts in the initial equilibrium state, with the magnetization M along the z-axis, so M_z = M and M_{xy} = 0. [B] Excitation state. A 90° RF pulse is applied, rotating M into the xy-plane, so M_z = 0 and M_{xy} = M. [C] Relaxation period. Over time, relaxation processes reduce the magnitude of M_{xy}. In panel C, T_2 and T_2^* dephasing are shown. [D] Refocusing pulse. A 180° x' RF pulse rotates the spins around the x'-axis. [E] Echo formation. As individual spins continue to precess at their respective ω, they rephase at TE, restoring M_{xy}. An MR signal is recorded as the magnetization is rephased. [A] Recovery. Over time, the system will relax to the equilibrium state, so M_z = M and M_{xy} = 0 and [B] a new experiment can be initiated.*

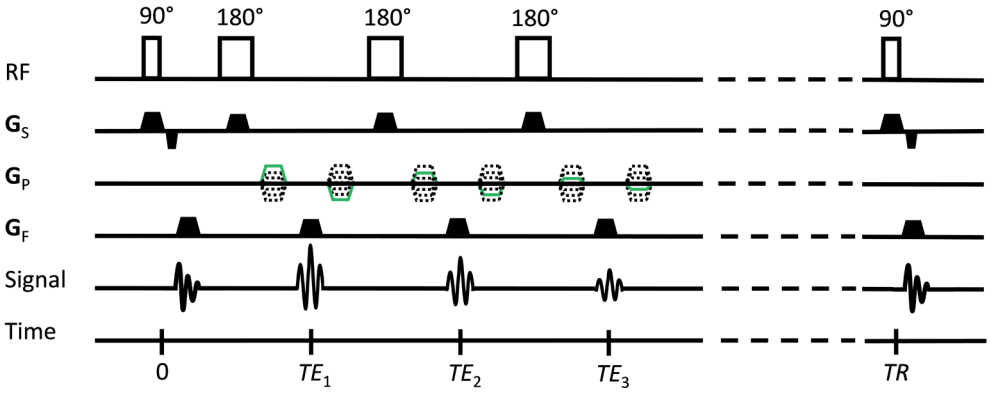

Figure 1.7 Rapid acquisition with relaxation enhancement (RARE) MRI sequence. *After the initial 90° RF excitation pulse, multiple 180° RF refocusing pulses are applied, each with a different phase encoding gradient. Consequently, MRI acquisition is significantly faster through the RARE MRI sequence, compared to the basic spin echo sequence shown in Figure 1.6, which employs a single phase encoding step per excitation cycle.*

Compared to the basic spin echo sequence utilizing one phase encoding step per excitation cycle, the RARE sequence is significantly faster. However, as the ETL increases, relaxation effects accumulate, leading to a progressive decline of the MR signal for each subsequent echo. This effect becomes more prominent at higher magnetic field strengths, where T_2 relaxation times tend to decrease[129,130]. Consequently, the effectiveness of very long ETL diminishes, rather leading to increased noise in the acquired data. Nonetheless, RARE provides a distinct advantage over fast gradient echo MRI sequences due to its inherent refocussing of transverse magnetization. 180° refocusing pulses correct for T_2^*-induced spin dephasing, responsible for susceptibility artifacts[131].This makes the RARE sequence less susceptible to artifacts from magnetic susceptibility compared to sequences based on gradient echo, a benefit that becomes even more pronounced at ultra-high magnetic field strengths where susceptibility artifacts tend to worsen[132]. This phenomenon is further elaborated in Section 1.3.5.2.

Additionally, a dominant observation in anatomical imaging with the RARE sequence is an atypical bright fat signal. This phenomenon is believed to stem from the utilization of echo spacings that disrupt the *J*-modulation dephasing pattern of lipid protons[133]. These unusual bright lipid signals can significantly affect MRI images through chemical shift displacement effects (see Section 1.3.5.2). Such artifacts misalign the fat signal, resulting in the merging of the fat signal with surrounding tissues. Therefore, implementing fat suppression methods in RARE is essential to mitigate these effects.

3.2.3 Ultra-fast data acquisition with echo planar imaging (EPI)

Echo planar imaging (EPI) is an ultra-fast method for MRI data acquisition[134]. An example of a basic spin echo EPI MRI sequence is shown in Figure 1.8. After the standard 90° RF excitation pulse and the 180° RF refocusing pulse, multiple gradient echoes are generated by the frequency encoding gradient and a train of short phase encoding gradient pulses, called blips, are utilized to fill the *k*-space. EPI MRI measurements filling the total *k*-space in a single excitation curve is commonly referred to as single shot EPI. In multi-shot EPI, the number of excitation cycles utilized to fill the *k*-space is referred to as the EPI factor, the echo train length, or shot factor.

Although the total MRI acquisition time is significantly reduced by EPI, EPI is highly sensitive to susceptibility artifacts, particularly as the magnetic field strength and the EPI factor increase[134]. This sensitivity can substantially limit the applicable EPI factor in UHF MRI, as discussed in Section 1.3.5.2. In this thesis, EPI is utilized to significantly reduce the total acquisition time of multi-shell diffusion tensor imaging measurements. These measurements inherently require

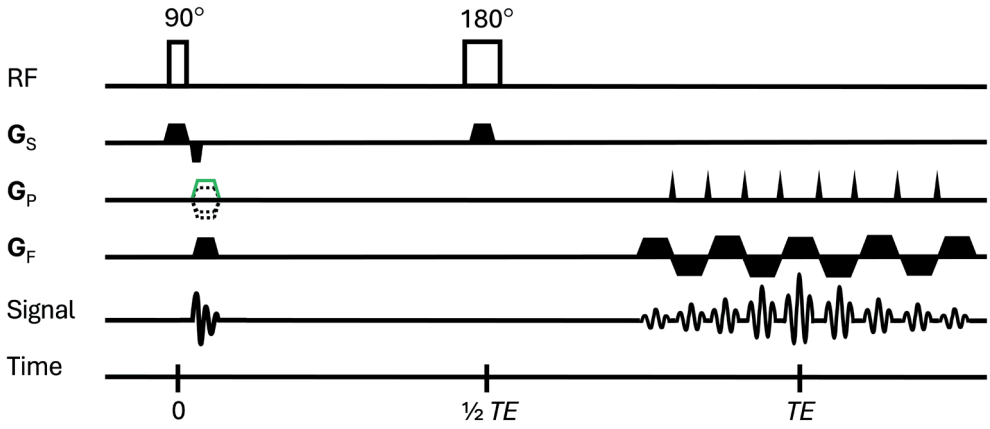

Figure 1.8 *Spin echo – echo planar imaging (EPI) MRI sequence for ultra-fast MRI data acquisition.*

extended durations due to their utilization of multiple diffusion-sensitizing factors (*b*-values) and diffusion-encoding directions (see Section 1.3.3.2).

3.2.4 T_1 and T_2 relaxation time estimation

The longitudinal and transverse relaxation times T_1 and T_2 in tissue depend on the chemical and physical environment in which molecules are present[135]. Relaxation times directly influence MRI sequence parameters, determining the optimal *TE* and *TR* needed to achieve sufficient signal-to-noise ratio (SNR) and desired MRI contrast. Furthermore, pathology can induce local changes in the microstructural environment and consequently modulate relaxation times. This is utilized in clinical applications to create contrast between healthy brain tissue and affected tissue, including tumours[136]. Additionally, quantitative analysis of relaxation times provides detailed information of the progression in microstructural changes in pathologies[135].

For the estimation of T_2 relaxation times, the work presented in this thesis relies on the multi-slice multi-echo (MSME) sequence[137], which is based on the Carr-Purcell-Meiboom-Gill (CPMG) sequence[138]. Although both the RARE MRI sequence (Figure 1.7) and the MSME MRI sequence (Figure 1.9) employ a train of 180° refocussing pulses, they obtain different results. These differences arise from the difference in their use of the MRI gradient systems. In RARE, the phase encoding gradient is employed to acquire multiple echoes each with different phases. This allows for anatomical imaging with short total scan time, as discussed in the previous chapter. In MSME, however, all echoes within a single excitation cycle are acquired with one phase encoding step. Instead, MSME utilizes the 180° refocussing echo train to

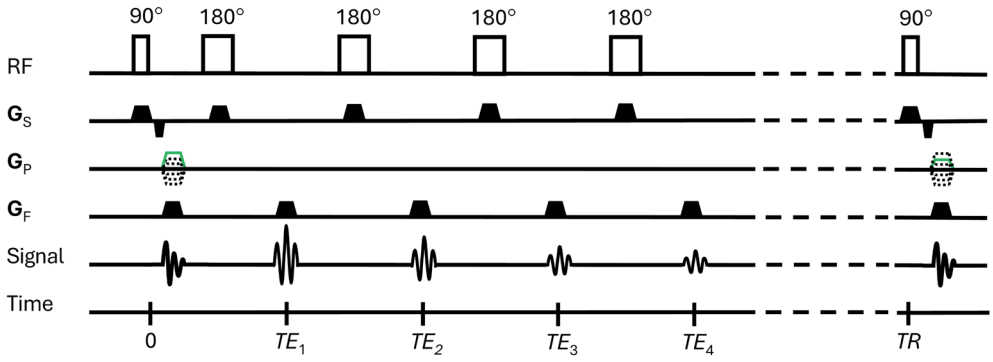

Figure 1.9 *Multi-slice multi-echo (MSME) MRI sequence. The MSME sequence is in the current thesis utilized for the estimation of T_2 relaxation times. The 180° refocusing echo train utilizes a single encoding gradient line per excitation cycle, allowing to acquire the exponential decay of the MR signal at increasing TE.*

monitor the progression of the signal intensity per voxel at increasing echo times. As stated previously, the 180° refocussing pulse compensates for the loss of coherence caused by T_2^* processes from local heterogeneities of the magnetic field, but not for the T_2 processes from molecular and atomistic interactions. Therefore, T_2 relaxation continues to evolve, and the signal intensities decrease with each new echo depending on the local T_2.

Figure 1.10A shows the signal loss progression in the brain area of an adult wild-type male zebrafish with increasing *TE*. The MR signal intensity decays exponentially and the transverse relaxation time T_2 is estimated through mono-exponential line fitting of the MR signal to

$$I_{\mathrm{TE}} = A + I_0 \cdot \exp^{\frac{-TE}{T_2}} \quad . \tag{1.4}$$

Here, I_{TE} is the MR signal intensity at *TE*, *A* is the absolute bias, and I_0 is the signal intensity at *TE* = 0. During data analysis of the MSME MR signal intensities, uneven echoes should be excluded as an extension of the workflow proposed by Milford *et al.*[139]. Inhomogeneities in the RF magnetic field $\mathbf{B}_1$ can locally lead to imperfect refocussing pulses (Φ < 180°)[140-142]. Consequently, the coherence losses caused by T_2^* processes are not fully compensated, negatively impacting the observed signal intensity of the echo. However, as the $\mathbf{B}_1$ inhomogeneities remain stable during the measurements, all even echoes fully compensate for T_2^* processes and thus represent T_2 relaxation. This effect can be significant, often resulting in a lower intensity for the first MSME echo compared to the second. Figure 1.10B shows the results of uncorrected data fitting, which includes all MSME echoes, and corrected data fitting, which excludes uneven MSME echoes. As shown, different T_2 are estimated by corrected and

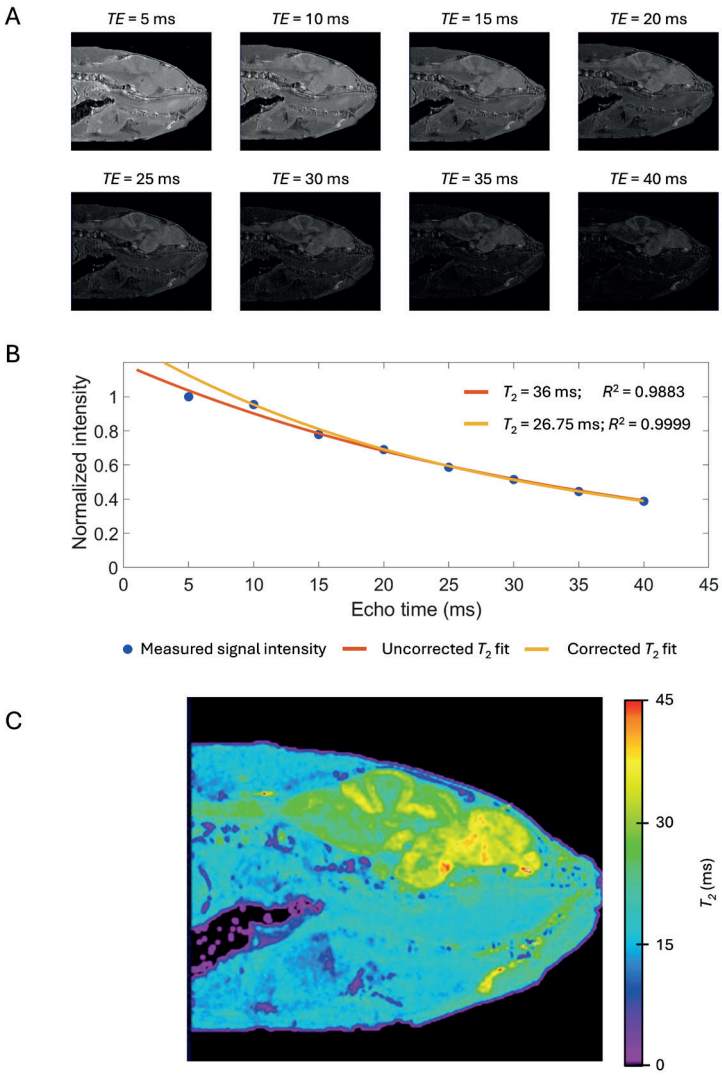

Figure 1.10 Utilization of the MSME MRI sequence for T_2 relaxation time estimation. [A] *MRI images of the zebrafish brain area, acquired with the multi-slice multi-echo (MSME) sequence at increasing TE. Image intensities were scaled to the first echo (TE 5 ms) for comparison of signal intensities.* ***[B]*** *Utilization of MSME data to estimate T_2 relaxation times. With increased TE, T_2 relaxation causes exponential decay in the signal intensity, described by $[I_{TE} = A + I_0 \cdot exp\ (-TE/T_2)]$. Mono-exponential data fitting is utilized to estimate local T_2 relaxation times. As stated by Milford et al. (2015)[139], uneven echoes should be excluded in data fitting. Both uncorrected data fitting, which includes all MSME echoes, and corrected data fitting, which excludes uneven MSME echoes, are shown here. In the current example, an area in the zebrafish pallium was selected for data analysis.* ***[C]*** *T_2 map of the zebrafish brain area. Acquisition details – Sample information: wild-type young adult male zebrafish, 3 months old, fixated in paraformaldehyde for 4 days – MRI hardware: Bruker vertical bore system (Bruker Biospin GmbH, Germany), $\boldsymbol{B}_0$ 17.6 T, Micro5 gradient system (Bruker Biospin GmbH, Germany), G_{max} 3 T/m – MSME parameters: TR 2500 ms, τ 5 ms, ns = 4, resolution 23 × 23 µm, and a slice thickness 200 µm.*

uncorrected data fitting, with improved fitting obtained by the corrected fitting method, as evident from the coefficient of determination (R^2). Additionally, Figure 1.10C shows a T_2 map constructed from MSME estimation on a voxel-to-voxel basis, providing a full overview of the T_2 times distribution in the zebrafish brain region.

T_1 relaxation times are estimated by monitoring the longitudinal magnetization $\mathbf{M}_z$ recovery, accomplished by measuring the MR signal at various repetition times. To reduce the total measurement time, the work in this thesis utilizes a sequence combining the RARE MRI sequence presented in Section 1.3.2.2 with variable repetition times (RAREVTR). The RAREVTR MRI sequence is shown in Figure 1.11.

Figure 1.12A shows the increasing signal intensity progression observed by measuring at increasing repetition times in the brain area of an adult wild-type male zebrafish. The exponential recovery of the longitudinal magnetization is shown in Figure 1.12B, utilizing the MR signal of an ROI selected in the pallium of the zebrafish brain. The longitudinal repetition time T_1 is estimated through mono-exponential line fitting of the MR signal to

$$I_{\mathrm{TR}} = A + I_0 \cdot \left(1 - \exp^{\frac{-TR}{T_1}}\right) . \tag{1.5}$$

Here, I_{TR} is the signal intensity at TR and I_0 is the signal intensity at TR = 0. Additionally, T_1 can be estimated on a voxel-by-voxel basis, for the construction of T_1 maps (see Figure 1.12C).

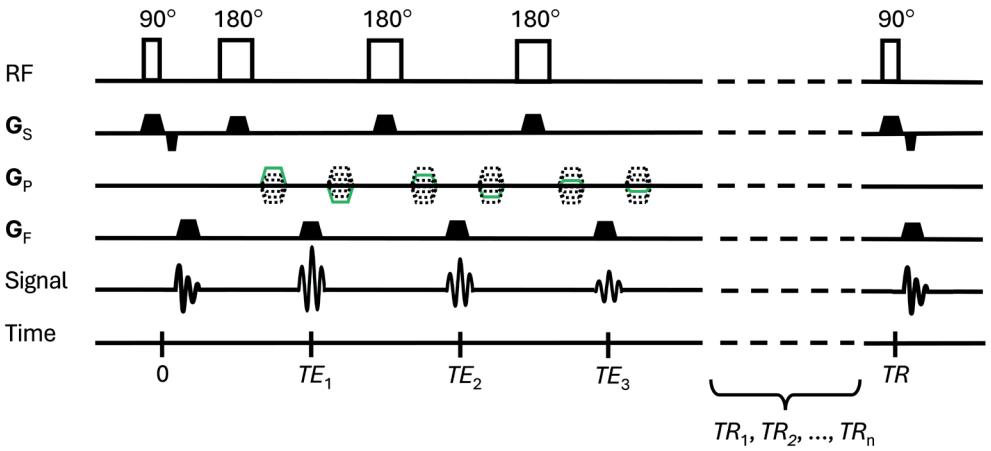

Figure 1.11 *RARE with variable repetition times (RAREVTR) MRI sequence for the estimation of T_1 relaxation times.*

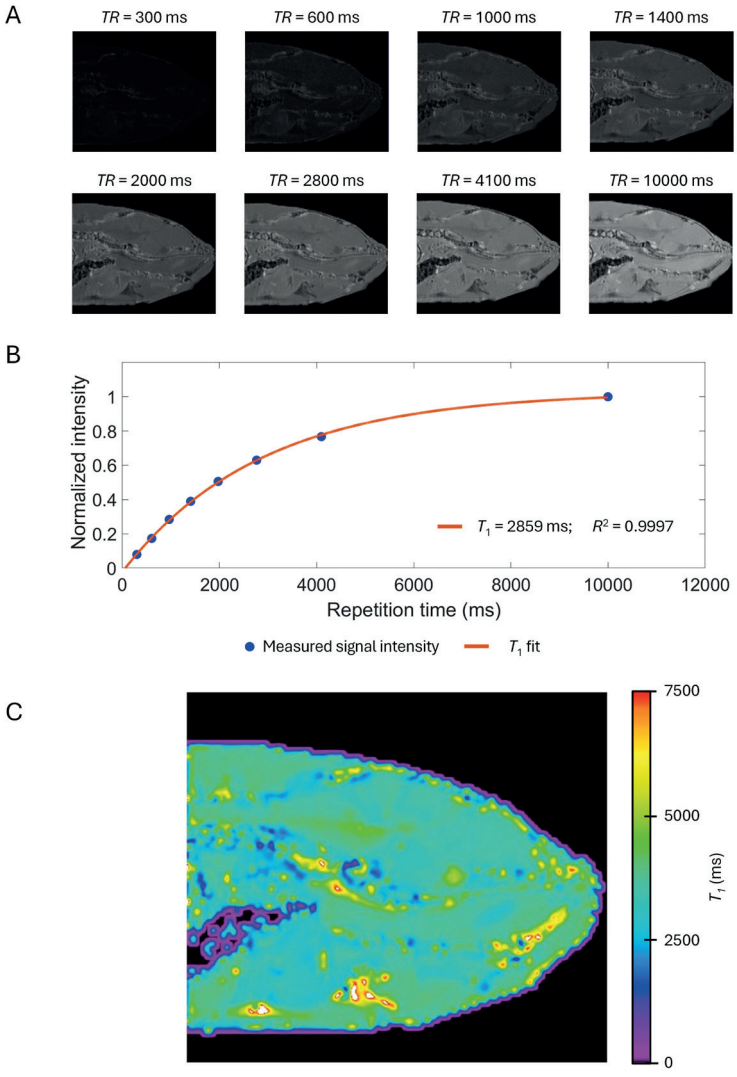

Figure 1.12 Utilization of the RAREVTR MRI sequence for T_1 relaxation time estimation. [A] *MRI images of the zebrafish brain area, acquired with the rapid acquisition with relaxation enhancement with variable repetition time (RAREVTR) MRI sequence at increasing TR. Image intensities were scaled to the longest repetition time echo (TR 10000 ms) for visualization of the longitudinal magnetization* $\mathbf{M}_z$ *recovery.* ***[B]*** *Utilization of RAREVTR data to estimate T_1 relaxation times. With increased TR, T_1 relaxation gives rise to exponential recovery with increasing TR, described by $[I_{TR} = A + I_0 \cdot (1- \exp(-TR/T_1))]$. Mono-exponential data fitting is utilized to estimate local T_1 relaxation times. Here, an area in the zebrafish pallium was selected for data analysis as example.* ***[C]*** *T_1 map of the zebrafish brain area. Acquisition details – Sample information: wild-type young adult male zebrafish, 3 months old, fixated in paraformaldehyde for 4 days – MRI hardware: Bruker vertical bore system (Bruker Biospin GmbH, Germany),* $\mathbf{B}_0$ *17.6 T, Micro5 gradient system (Bruker Biospin GmbH, Germany) G_{max} = 3 T/m – RAREVTR parameters: TR = 300, 600, 1000, 1400, 2000, 2800, 4100, or 10000 ms, TE = 3 ms, ns = 2, resolution 47 × 47 µm, and a slice thickness 200 µm.*

3.3 Diffusion-based MRI

Molecular diffusion describes the spontaneous and random movement of molecules, known as Brownian motion, driven by the thermal energy of molecules. This phenomenon was for the first time thoroughly elucidated by Albert Einstein in 1905[143]. Diffusion-based MRI stands out as a unique tool with the extraordinary ability to non-invasively monitor the random movements of water within biological tissue[144]. Particularly in the realm of brain imaging, dMRI has demonstrated its invaluable utility in investigating neurological disorders. However, the versatility of dMRI extends beyond neuroimaging to applications in other fields including oncology[145], musculoskeletal imaging[146], and cardiovascular research[147], making it a powerful tool in modern medical diagnostics and research. dMRI offers a diverse array of non-invasive analytical tools that surpass the capabilities of conventional MRI and other clinical techniques, enabling unprecedented insights into the complexities of brain structure and connectivity. In its most fundamental form, dMRI provides additional contrast beyond those provided by T_1, T_2, and proton density differences, exhibiting exceptional sensitivity in both detecting and precisely localizing acute ischemic brain lesions[148]. Furthermore, fundamental dMRI is utilized for estimating the apparent diffusion coefficient (*ADC*), quantifying the diffusion rate of water molecules within tissues, thereby providing information about tissue microstructure and integrity[149-151]. Advanced dMRI techniques offer rich data by capturing higher-dimensional information, including estimation of the diffusivity anisotropy[152], deviation from Gaussian distribution[153], axonal diameter[154], and white matter connectivity[155]. In this thesis, various dMRI techniques were utilized for the analysis of the zebrafish brain including its pathology; diffusion-weighted imaging (DWI), diffusion tensor imaging (DTI), diffusion kurtosis imaging (DKI), and diffusion tractography. The basic principles of these techniques are discussed in this section.

3.3.1 Diffusion-weighted imaging

DWI is the most fundamental diffusion-based MRI technique, first described by Le Bihan *et al.* in 1986[156], nowadays vastly utilized in clinical MRI to generate diffusion-based MRI contrast or to estimate local *ADC*[157]. Figure 1.13A shows the spin echo DWI sequence. Diffusion sensitivity is introduced in MRI through its gradient system $\mathbf{G}_{diff}$, utilized on both sides of the 180° RF refocussing pulse. The "dephasing" $\mathbf{G}_{diff}$ applied prior to the 180° RF refocussing pulse, induces phase variations across spins in three dimensions, linking spin phase to their spatial distribution within the sample. For stationary nuclei, the rephasing $\mathbf{G}_{diff}$ applied after the 180° RF refocussing pulse would reinstate the spin phase, yielding an MR signal intensity similar to a conventional spin echo sequence. However, thermally induced random motions cause the nuclei to move between the dephasing and rephasing $\mathbf{G}_{diff}$. As a result, the rephasing $\mathbf{G}_{diff}$ will not fully rephase those spins that moved away from their starting position, resulting in MR signal loss. Consequently, the observed MR signal intensity reflects local diffusivity: samples

with high diffusivity exhibit weak signal intensity, whereas those with low diffusivity display strong signal intensity. This is visualized in Figure 1.13B.

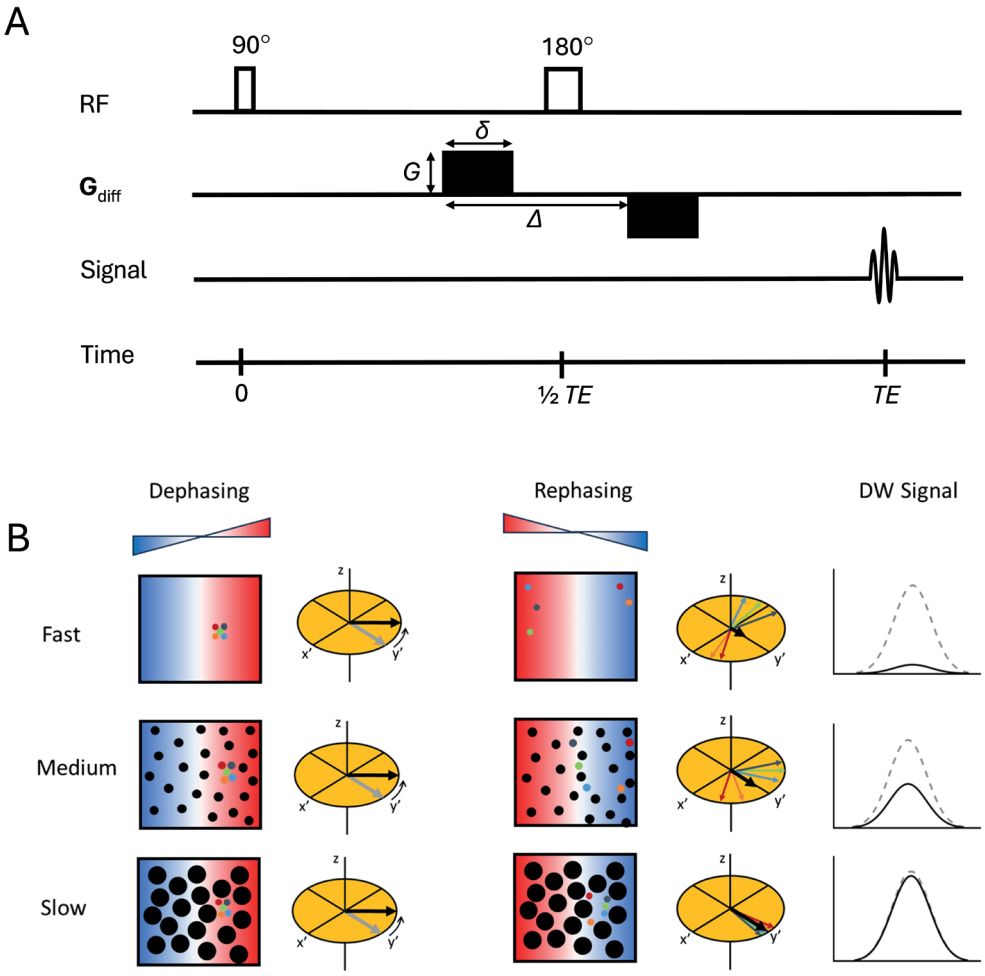

Figure 1.13 [A] *Pulse sequence of a basic diffusion-based MRI sequence. [B] Effect of diffusivity on observed signal as a consequence of the dephasing and rephasing gradient pulses. A sample with a high diffusivity will lead to a low diffusion-weighted (DW) signal, while a sample with a low diffusivity will lead to a high DW signal. In this example, only the effect of dephasing and rephasing for one of the three gradient directions is visualized.*

The total diffusion weighting of a dMRI experiment is determined by the gradient amplitude (*G*), gradient duration (*δ*), and gradient time interval (*Δ*). Conventionally, these are summarised in the *b*-value, according to

$$b = \gamma^2 \cdot G^2 \cdot \delta^2 \cdot \left(\Delta - \frac{\delta}{3} \right). \tag{1.6}$$

In DWI, the diffusion-weighted MR signal is measured at a specific, or at various *b*-values. In this work, the DWI methods utilize fixed values for *δ* and *Δ*, and the *b*-values are set by changing the gradient strengths *G*. A lower *b*-value signifies minimal diffusion weighting, whereas a higher *b*-value signifies heightened diffusion weighting.

Figure 1.14A shows the loss of MR signal intensity at increasing *b*-values, indicating strong diffusion weighting is applied. Notably, diffusion-weighted MRI enhances the contrast between the zebrafish brain and its surroundings compared to conventional MRI techniques discussed earlier. This heightened contrast arises from the diminished water diffusivity within brain tissue relative to other tissues, accentuating tissue boundaries. Figure 1.14B demonstrates how the local diffusion rate of water molecules can be estimated by fitting the MR signal to a mono-exponential decay function at increasing *b* according to

$$I_{\mathrm{b}} = A + I_0 \cdot \exp^{-b \cdot ADC}. \tag{1.7}$$

Here, I_b is the signal intensity at *b* and I_0 is the signal intensity at b_0. *ADC* analysis performed on a voxel-to-voxel basis generates *ADC* maps as demonstrated in Figure 1.14C.

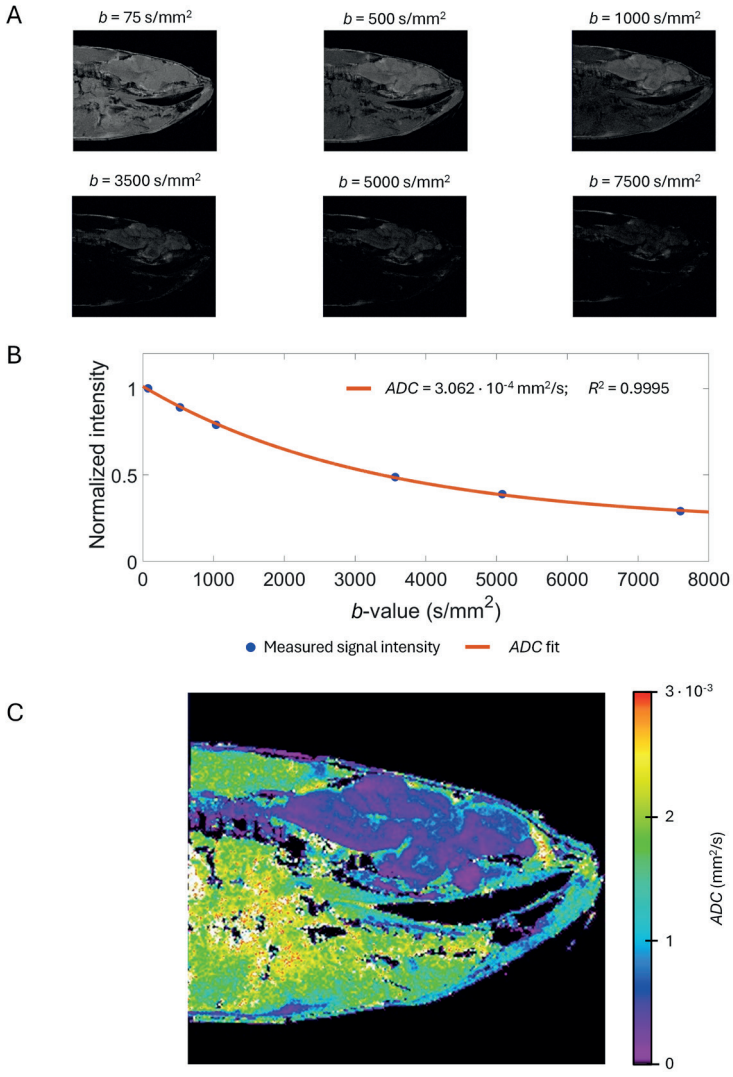

Figure 1.14 Utilization of the DWI MRI sequence for apparent diffusion coefficient estimation. [A] *MRI images of the zebrafish brain area, acquired with the spin echo diffusion-weighted imaging (DWI) MRI sequence at increasing b-values. Image intensities were scaled to the lowest diffusion-weighting image (b = 75 s/mm²) for visualization MR signal loss by diffusion.* ***[B]*** *Utilization of DWI data to estimate ADC through mono-exponential line fitting. With increased b, diffusion processes cause an exponential decay of the MR signal, described by [$I_b = A + I_0 \cdot \exp(-b \cdot ADC)$]. Here, an area in the zebrafish pallium was selected for data analysis as example.* ***[C]*** *ADC map of the zebrafish brain area. Acquisition details – Sample information: wild-type young adult male zebrafish, 3 months old, fixated in paraformaldehyde for 4 days – MRI hardware: Bruker vertical bore system (Bruker Biospin GmbH, Germany),* $\boldsymbol{B}_0$ *17.6 T, Micro5 gradient system (Bruker Biospin GmbH, Germany)* G_{max} *3 T/m – DWI parameters: TR = 1000 ms, TE = 20.2 ms, ns = 4, resolution 23 × 23 µm, slice thickness 200 µm, δ = 4 ms, Δ = 10 ms, b-values 75, 500, 1000, 3500, 5000, or 7500 s/mm².*

3.3.2 Diffusion tensor imaging

In a free medium, such as free flowing water, the Brownian motion induced displacement of molecules is described by a Gaussian distribution towards all three spatial dimensions. The distance travelled by these molecules is described by the diffusion coefficient *D*, depending on the molecular mass, the temperature, and the viscosity of the medium. A diffusion ellipsoid of such a medium is isotropic and the eigenvalues (λ_1, λ_2, λ_3) of its eigenvectors ($\boldsymbol{\varepsilon}_1$, $\boldsymbol{\varepsilon}_2$, $\boldsymbol{\varepsilon}_3$) identical; $\lambda_1 = \lambda_2 = \lambda_3 = D$ (Figure 1.15A). Biological tissue contains cell membranes, fibres, macromolecules, and other obstacles hindering the motion of its water content. Anisotropic diffusion, characterised by directional preferences, is observed in many types of tissue, including muscle[158], kidney[159], liver[160], and heart[147] tissue. However, the most profound instances of anisotropic diffusion occur in white matter structures of the spinal cord[161] and brain[162]. The long axonal fibre bundles of white matter create directional preferences, amplified by their myelin insulation. The myelin sheet acts as a barrier, confining water movement to parallel trajectories along the axons while hindering perpendicular diffusion. Consequently, the diffusion ellipsoid and tensor in biological tissues exhibit anisotropic characteristics, where the eigenvalues of the diffusion tensor vary accordingly, with $\lambda_1 > \lambda_2 > \lambda_3$ (Figure 1.15B).

DTI is an advanced dMRI technique, providing orientational information of diffusion characteristics in tissue. Whereas DWI assumes isotropic diffusion, DTI measures the MR signal in various diffusion-encoding directions to construct the diffusion ellipsoid and tensor matrix **D**. **D** has six degrees of freedom, necessitating the MR signal to be determined across a minimum of six orthogonal orientations[163]. Yet, employing additional diffusion-encoding

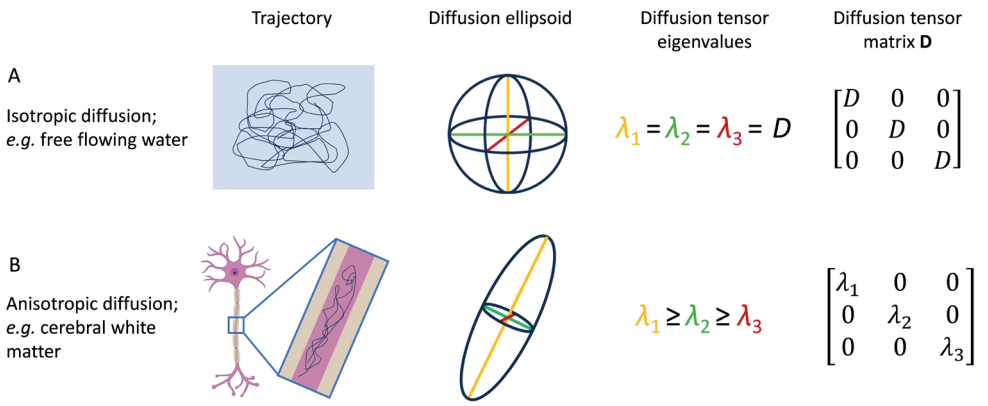

Figure 1.15 *The diffusion trajectories and corresponding diffusion ellipsoid, diffusion tensor eigenvalues, and diffusion tensor matrix* ***D*** *in* ***[A]*** *isotropic diffusion, e.g. free flowing water and* ***[B]*** *anisotropic diffusion, e.g. white matter structures.*

directions significantly enhances the data quality[164]. The diffusion tensor eigenvalues are utilized to estimate the diffusion tensor metrices; the axial diffusivity ($D_{\shortparallel}$), the radial diffusivity ($D_{\perp}$), the mean diffusivity (*MD*), and the fractional anisotropy (*FA*).

$D_{\shortparallel}$ represents the diffusivity along the principal eigenvector $\boldsymbol{\varepsilon}_1$ and is represented by the principal eigenvalue λ_1, $D_{\perp}$ is the average diffusivity along the two non-principal eigenvectors $\boldsymbol{\varepsilon}_2$ and $\boldsymbol{\varepsilon}_3$, *MD* is the average diffusivity along $\boldsymbol{\varepsilon}_1$, $\boldsymbol{\varepsilon}_2$, and $\boldsymbol{\varepsilon}_3$, and *FA* represents the degree of anisotropy of the water diffusion between the eigenvectors, ranging from 0 – 1. Hence,

$$D_{\shortparallel} = \lambda_1 \,, \tag{1.8}$$

$$D_{\perp} = \frac{\lambda_2+\lambda_3}{2} \,, \tag{1.9}$$

$$MD = \frac{\lambda_1+\lambda_2+\lambda_3}{3} \,, \qquad \text{and} \tag{1.10}$$

$$FA = \frac{\|D-MD\cdot I^{(2)}\|}{\|D\|} = \sqrt{\frac{\frac{3}{2}\left((\lambda_1-MD)^2+(\lambda_2-MD)^2+(\lambda_3-MD)^2\right)}{{\lambda_1}^2+{\lambda_2}^2+{\lambda_3}^2}} \,. \tag{1.11}$$

Here, $I^{(2)}$ represents the fully symmetric rank 2 isotropic tensor, while $||..||$ denotes the application of the Frobenius norm[165].

Nowadays, DTI is extensively utilized in clinical studies to monitor pathologically induced microstructural changes in the brain. Various neurological disorders including Alzheimer's disease[166], Huntington's disease[167], and Parkinson's disease[168] show significant changes in the diffusion tensor metrices correlating to the pathological progression. However, non-neurodegenerative brain disorders, including strokes[169], brain tumours[170], and attention deficit hyperactivity disorder (ADHD)[171] also show clear changes in the diffusion tensor metrices. Broadly, it is understood that $D_{\shortparallel}$ is a potential marker for axonal degeneration, $D_{\perp}$ is particularly sensitive to shifts in white matter myelin integrity, *MD* serves as a potential indicator for edema and cellular proliferation in neoplastic growth, and *FA* stands out as a widely utilized marker for assessing the integrity of white matter structures[163,172,173]. However, it's important to approach the direct correlation of specific changes in diffusion tensor metrics with potential microstructural alterations cautiously. Such associations should be carefully validated with additional techniques, as various factors can induce similar changes and might cause misinterpretation of DTI data[174].

3.3.3 Diffusion kurtosis imaging

DWI and DTI operate under the assumption that diffusivity within the brain conforms to a Gaussian distribution, assuming a mono-exponential decay of the MR signal with increasing *b*-value as described by equation 1.7, thereby oversimplifying the actual complexity of diffusivity in brain tissue[175]. For both grey matter and white matter this assumption was proven to be invalid at high *b*-values, when dMRI becomes more sensitive towards shorter diffusion distances[153]. Consequently, beyond highlighting DWI's and DTI's inability to fully utilize all available information provided by MR diffusion measurements for understanding tissue microstructure, this also restricts the use of high *b*-values in DWI and DTI. High *b*-values introduce deviations from the mono-exponential fit used by DTI, thereby introducing deviation in the estimated DTI metrics through line-fitting[153]. Furthermore, DTI fails to consider the complexity of biological tissue, especially in the brain, such as crossing fibres, which have a direct influence on estimated diffusion tensor metrics potentially leading to incorrect conclusions[174].

In the realm of dMRI, the deviation of water diffusion displacement from a normal distribution is referred to as kurtosis. A kurtosis of 0 indicates the diffusion profile perfectly follows a normal Gaussian distribution, expected for free-flowing water. In biological tissue, a positive kurtosis (kurtosis > 0) is anticipated, indicating diffusion initially occurs at a rapid pace, gradually slowing down as water molecules increasingly interact with cellular structures. Elevated kurtosis values indicate greater obstacles to regular diffusion and heightened complexity[175].

DKI is a dMRI method building upon DTI to account for non-Gaussian diffusivity towards various diffusion-encoding directions. Diffusion kurtosis is characterised by a fully symmetrical 3 × 3 × 3 × 3 diffusion tensor matrix **W** with 15 degrees of freedom, necessitating a minimum 22 MR images, taken across at least 15 diffusion-encoding directions recorded at a minimum of 3 unique *b*-values[176]. Moreover, unlike DWI and DTI, DKI mandates the use of high *b*-values (> 2000 s/mm²), as diffusion at low *b*-values are predominantly influenced by Gaussian diffusion[177]. A full explanation of the methodology describing the construction of **W** is provided by Veraart *et al.*[178].

From **W**, the diffusion kurtosis metrics can be estimated; the axial kurtosis ($K_\parallel$), the radial kurtosis ($K_\perp$), the mean kurtosis (*MK*), and the kurtosis fractional anisotropy (*KFA*). $K_\parallel$ represents the kurtosis along the principal eigenvector $\boldsymbol{\varepsilon}_1$ thus in the same orientation as $D_\parallel$, $K_\perp$ is the average kurtosis along the two non-principal eigenvectors $\boldsymbol{\varepsilon}_2$ and $\boldsymbol{\varepsilon}_3$ thus in the same orientations as $D_\perp$, *MK* is the average kurtosis along $\boldsymbol{\varepsilon}_1$, $\boldsymbol{\varepsilon}_2$, and $\boldsymbol{\varepsilon}_3$, and *KFA* represents the degree of anisotropy of the kurtosis.

3.3.4 Diffusion MRI tractography

Diffusion tractography, also known as diffusion fibre tracking, is uniquely distinguished as the sole non-invasive method capable of mapping intricate white matter connections in the brain by leveraging the directional preferences of water diffusion within axons, offering invaluable insights into neural connectivity and function. Strictly ordered white matter fibre bundles in combination with their myelin sheets give rise to a high order of directional diffusion preference of the water molecules inside their axons. The applications of diffusion MRI tractography include white matter structure visualization and identification[179] assessment of white matter deformation as a consequence of tumours[180], preoperative assessment and strategizing[181], and detection of the early stages of neurodegenerative diseases[182].

In diffusion MRI tractography the dMRI signal is collected towards multiple diffusion-encoding directions for each voxel, revealing local fibre orientations. Diffusion MRI tractography utilizes tracking algorithms to translate local fibre orientations to pathways, of which the first were introduced in 1998[183,184]. Today, there exists a multitude of diffusion MRI tractography algorithms and data processing tools, too numerous to cover comprehensively in this work. Broadly, diffusion MRI tractography algorithms are categorised into deterministic or probabilistic approaches[185]. In their most basic form, tractography algorithms are deterministic. For each voxel, a single fibre orientation is estimated, and pathways are generated based on the principal eigenvectors of the diffusion tensors[186]. However, deterministic algorithms are highly susceptible to signal noise and artifacts. Furthermore, they cannot consider the crossing or closely passing of white matter fibres in a single voxel, which can lead to erroneous or false fibre tracts[187,188]. Probabilistic diffusion tractography algorithms utilize seed points, which define ROIs in the brain through which a large distribution of trajectories is generated. The regions in the brain exhibiting a high density of trajectories are considered to possess an elevated likelihood to be connected to the seed point[185]. Diffusion MRI tractography described in the current work is based on the probabilistic approach proposed by Dhollander *et al.*[189]. It utilizes constrained spherical deconvolution (CSD) to generate fibre orientation distribution functions (fODF) based on the response function of the white matter fibre populations. In short, a white matter response function is generated based on the diffusion-weighted MR signal from voxels assumed to contain a single fibre orientation. The response function is used to generate fODF's through CSD by relating the fODF coefficient vectors, the vectors of the diffusion-weighted MR signal intensities, and the CSD operation. This process transforms the CSD operation into a linear least-squares problem[190]. Following this, a probabilistic algorithm is employed wherein, at each step of the streamline, random samples are drawn from the local fODF via trilinear interpolation. This workflow offers the advantage of integrating biophysical data, which helps mitigating the occurrence of false-positive tracks from grey matter tissue[190,191]. The exploration of diffusion MRI tractography in the zebrafish brain is an

emerging field, with Ullmann *et al.*'s publication[192] being the only other known reference so far. The compact size of the zebrafish brain, coupled with the inherent low SNR of MRI techniques presents considerable challenges. In this work, diffusion MRI tractography primarily aims to visually map the exact localization of white matter structures within the zebrafish brain, allowing to examine their integrity through DTI and DKI metrics.

3.4 Localized magnetic resonance spectroscopy

^{1}H MRS is a unique technique offering a window into the local biochemical composition of tissue. Where traditional NMR provides ^{1}H NMR spectra of the whole sample inside the scanner, localized ^{1}H MRS allows for *in vivo* selection of regions by utilization of the MRI gradient systems. For the brain, MRS enables the non-invasive detection and quantification of various cerebral metabolites crucial for understanding brain function and pathology. Predominant cerebral metabolites detectable with localized ^{1}H MRS in the human brain include glutamate and GABA, two important neurotransmitters in the brain providing valuable insights into the brain function and health[193,194]. Specific metabolites may serve as markers for cell types, and NAA, primarily found in neuronal cell bodies and axons, stands as a promising indicator for tracking neuronal integrity[195]. Conversely, m-Ins, mainly located in glial cells, serves as a potential marker for osmotic stress or neuroinflammation[196].

Although various sequences are available for performing localized one-dimensional ^{1}H MRS, including stimulated echo acquisition mode (STEAM)[197], image selected *in vivo* spectroscopy (ISIS)[198], and localization by adiabatic selective refocusing (LASER)[199], the point resolved spectroscopy (PRESS) sequence is the most conventional method applied in MRS[200]. The PRESS sequence, visualized in Figure 1.16A, utilizes two spin echoes with three orthogonal slice selective RF pulses (90° - 180 ° - 180°). At the intersection of the three slices (fig 1.16B) the free induction decay (FID) is captured and converted to the frequency domain using Fourier transformation, providing the localized ^{1}H MRS spectra (fig 1.16C). Prior to the initial 90° RF excitation pulse, outer volume suppression (OVS) and water suppression (WS) pulses are typically applied (see fig 1.16A). OVS selectively removes signals originating from outside the selected ROI. This technique is commonly employed to suppress lipid signals, which significantly overlap with important cerebral metabolites such as lactate and NAA. OVS utilizes three repetitions of six narrow suppression slices positioned parallel to the voxel surface. OVS reduces the need for high gradient spoilers in the PRESS sequence, thereby lowering the minimum *TE*. Additionally, MRS often necessitates the usage of water suppression pulses. The water signal in ^{1}H MRS spectra is typically several orders of magnitude stronger than signals from metabolites of interest. This dominant water signal can obscure the detection and accurate quantification of these metabolites. By suppressing the water signal, MRS can achieve a clear and precise measurement of low concentration metabolites, enhancing the

overall quality and reliability of the spectral data. In the current work, water suppression is achieved through the variable pulse power and optimized relaxation delays (VAPOR) pulse sequence, consisting of 7 RF pulses with variable pulse powers and optimized relaxation delays for excellent water suppression with little sensitivity for T_1 and $\mathbf{B}_1$ inhomogeneities.

3.5 MRI and MRS at ultra-high magnetic fields

Terms like "ultra-high field" or "ultra-strong gradient" are inherently relative to the user's perspective. In clinical MRI, a 7 T field for human imaging is considered ultra-high, as are gradients of 300 mT/m. By comparison, systems operating at 17.6 T and 28.2 T with gradient strengths (G_{max}) of 3 T/m would need to be described with even more emphatic terms, such as "super-ultra-high". To provide clarification on the term usage in this thesis, distinction needs to be created between different MRI research fields. Commonly, these are made between three

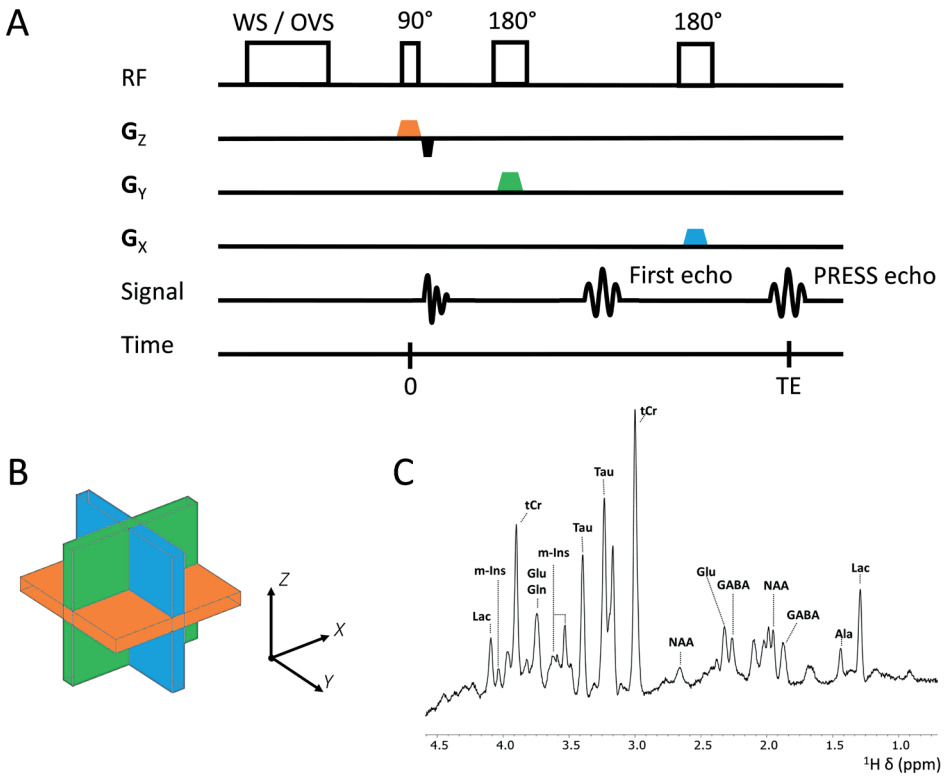

Figure 1.16 [A] *Point resolved spectroscopy (PRESS) MRI sequence.* ***[B]*** *Each of the three RF pulses (90°-180°-180°) is accompanied by a slice selective gradient pulses perpendicular to each other. The region where the three slices overlap, the ROI is selectively excited and* ***[C]*** *an MRS spectrum is recorded.*

main groups: clinical MRI, pre-clinical MRI, and micro-MRI, also known as MR microscopy. In this thesis, micro-MRI systems are employed and magnetic field strengths above 14.1 T (600 MHz) are regarded as ultra-strong, for they fall outside the range of more commonly used field strengths (7 T – 14.1 T). However, we acknowledge that recent hardware developments, such as the availability of 28.2 T (1.2 GHz) for imaging, may alter this perspective to some extent.

3.5.1 SNR and relaxation times

The push to employ higher magnetic field strengths in MRI and MRS primarily stems from the enhanced SNR[201] and improved spectral resolution achieved at elevated $\mathbf{B}_0$. Particularly in MRS, higher magnetic fields have greatly enhanced spectral resolutions, facilitating better identification and quantification of metabolites[202]. Metabolites that exhibit significant spectral overlap at lower fields may become completely separable at higher fields. Moreover, the increased SNR enables the use of smaller ROIs, facilitating metabolic exploration in finer tissue areas. Often, the relation $SNR \sim B_0^{7/4}$ is cited[203], although, in practice, experimentally comparing SNR across different magnetic fields is challenging[201].

Despite the clear benefits of increased SNR and enhanced spectral resolution, using ultra-high magnetic fields comes with specific challenges that require method adaptation. One major challenge is the influence of $\mathbf{B}_0$ on the relaxation times T_1 and T_2. T_1 relaxation time increases with $\mathbf{B}_0$, while the differences in T_1 between different tissues decrease. This leads to a theoretical reduction in T_1-based contrast at higher field strengths, but the practical increase in SNR at higher $\mathbf{B}_0$ also enhances the contrast-to-noise ratio (CNR). Moreover, longer T_1 relaxation times at elevated $\mathbf{B}_0$ require a longer TR to ensure proper recovery of longitudinal magnetization between RF pulses. However, the improved SNR and CNR at higher field strengths result in a significantly shorter total acquisition time[201].

Regarding T_2 relaxation times, they are theoretically expected to be unaffected by the magnetic field strength[204]. However, in practice, the T_2 relaxation times of biological tissues decrease significantly with increasing $\mathbf{B}_0$[129,130]. Longer T_2 relaxation times are preferred, as the MR signal decays exponentially with T_2. This necessitates the use of shorter echo times at higher $\mathbf{B}_0$ to avoid losing the SNR improvement provided by the increased magnetic field strength.

3.5.2 MRI artifacts at UHF

A common challenge during MRI data acquisition is the presence of MRI artifacts[205]. MRI artifacts are distortions or anomalies in MRI images that can potentially result in misdiagnosis or misinterpretation of the MRI data. There are various types of MRI artifacts, each with its own unique origin and specific methods to reduce their impact on the data. Some commonly observed examples of MRI artifacts include motion artifacts[206], chemical shift displacement

artifacts[207,208], aliasing artifacts[209], Gibbs/truncation artifacts[210], and susceptibility artifacts[211]. In this discussion, we will specifically focus on chemical shift displacement artifacts and susceptibility artifacts due to their dependence on the strength of the applied magnetic field.

Chemical shift displacement effects

Chemical shift displacement effects, also known as chemical shift misregistration or chemical shift artifacts, were first described in 1984 through the observation of the fat signal shift[207]. The chemical shift displacement (s_δ) depends on $\mathbf{B}_0$ and the field gradient strengths[208]. Chemical shift displacement artifacts arise along the frequency encoding gradient direction, where the gradient causes variations in Larmor frequencies within columns of the selected slice (see Figure 1.17A). Consequently, the Larmor frequency of water molecules, which predominantly contribute to the signals observed in MRI, varies depending on their position, $\mathbf{B}_0$, and the applied gradient strength. For instance, with an excitation bandwidth of 50 kHz and a field of view of 6 × 6 mm, the gradient strength is approximately 8333 Hz per mm. This implies that for every millimetre distance in the sample, the ^{1}H Larmor frequency varies by 8333 Hz (see Figure 1.17A). However, due to the broad excitation bandwidths utilized, not only the ^{1}H signal of water is excited but also signals from various other metabolites. These compounds do not precess with the same Larmor frequency as water but at a frequency depending on $\mathbf{B}_0$. For example, at 28.2 T (1.2 GHz), the Larmor frequency difference between water protons and lipid protons is approximately 4080 Hz. Consequently, during data processing, the lipid signals are assumed to originate from a position that corresponds to a shift of 4080 Hz from their true position (see Figure 1.17B), or approximately 0.5 mm with the specified parameters. This results in the mismapping of the fat signal commonly observed in anatomical MRI (see Figure 1.17C). Although the absolute magnitude of chemical shift displacement artifacts is reduced by the increased gradient strengths applied in UHF MRI, the significantly improved spatial resolution of these systems results in these artifacts still posing a significant challenge during MRI data processing. Increasing the gradient bandwidth can help mitigate these issues, although fat-suppression is often the easiest solution.

Beyond anatomical imaging, single voxel ^{1}H localized MRS also experiences significant effects from chemical shift displacement. This displacement occurs in three directions due to the way the ROI is selectively excited (see Figure 1.16A). As a result, the MRS signal of any metabolite not exactly positioned at the excitation frequency—often chosen at 4.7 ppm—originates not from the ROI but from a shifted position depending on its Larmor frequency, $\mathbf{B}_0$, and the applied gradient strengths. This effect can become pronounced if the measurement parameters are not sufficiently optimized. For instance, at 28.2 T (1.2 GHz), using excitation pulses of 4200 Hz and an ROI of 1 × 1 × 1 mm, s_δ = 0.97 mm in the *x*, *y*, and *z* axes (see Figure 1.17D). Consequently, hardly any of the observed lipid signals originate from the selected ROI. Although OVS helps

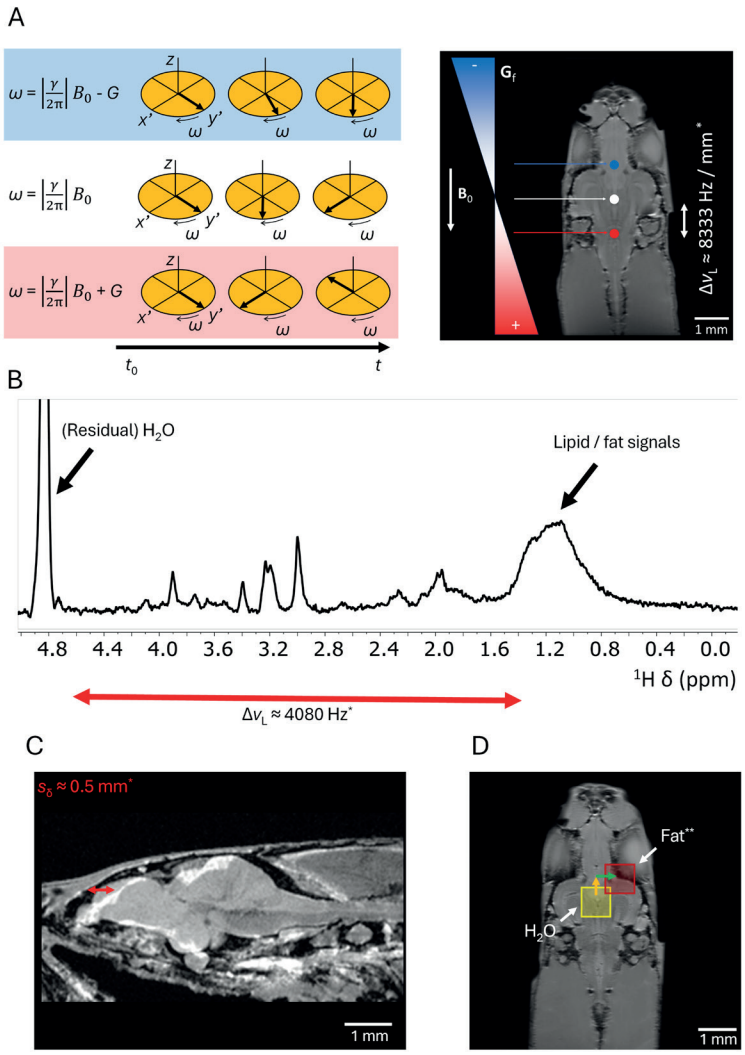

Figure 1.17 Chemical shift displacement artifacts [A] *In the frequency encoding direction, the Larmor frequency of the spins are modified relative to* $(\gamma/2\pi)B_0 \pm G_{local}$*. These variations in Larmor frequency are utilized for image reconstruction. Chemical shift displacement artifacts occur when the Larmor frequencies of metabolites differ from the excitation frequency. During image reconstruction, this frequency difference is erroneously attributed to the gradient rather than the actual frequency difference, leading to incorrect visualization of the metabolite signals.* ***[B]*** *For example, at 28.2 T the difference in the Larmor frequency of water protons and lipid protons is approximately 4080 Hz*.* ***[C]*** *In RARE, this results in significant MR lipid chemical shift displacement artifacts of approximately 0.5 mm*.* ***[D]*** *In single voxel localized MRS, chemical shift displacement effects cause the signals of metabolites that do not match the excitation frequency to originate from a spurious location. ** s_δ *for fat in RARE estimated assuming* B_0 *= 28.2 T / 1200 MHz, a gradient bandwidth of 50 kHz, excitation frequency of 4.7 ppm, and an ROI of 6 × 6 mm resulting in* G_F *= 8333 Hz/mm. *** s_δ *for fat in PRESS estimated assuming* $\boldsymbol{B}_0$ *= 28.2 T / 1200 MHz, excitation bandwidths of 4200 Hz, excitation frequency of 4.7 ppm, and an ROI of 0.8 × 0.8 × 0.8 mm.*

to suppress signals from outside the ROI, the signal intensities observed for metabolites with different chemical shifts compared to the excitation frequency are significantly reduced. To mitigate this effect, it is essential to increase the gradient strength and optimize the excitation frequency for the metabolites of interest. Properly optimized measurement parameters can significantly reduce the impact of chemical shift displacement, improving the accuracy and reliability of the MRS data.

Magnetic susceptibility artifacts

Magnetic susceptibility refers to the tendency of a material to become magnetized when exposed to an external magnetic field[211]. A distortion in the primary magnetic field arises at the interface of two materials with different magnetic susceptibility. This distortion in the primary magnetic field causes a change in the local Larmor frequency, resulting in T_2^* dephasing signal loss and a misplacement of the MR signal in the phase encoding direction. Consequently, the characteristic pattern of a susceptibility artifact is observed, which is an area without signal next to a bright region as a consequence of misplaced signal accumulation (see Figure 1.18). Common places showing susceptibility artifacts in human MRI include the paranasal sinuses and the interface between bones and soft tissue[211]. In the paranasal sinuses, these artifacts stem from susceptibility differences between paramagnetic molecular oxygen in air and soft tissue, while in the bone-soft tissue interface, they are primarily due to the presence of diamagnetic calcium salts in bones. Additionally, just as paranasal sinuses can cause susceptibility artifacts, air bubbles can also induce significant artifacts, particularly in UHF micro-MRI, and should therefore be minimized whenever possible. Several imaging parameters contribute to the severity of susceptibility artifacts. First, the magnetization M (A/m) of a material increases linearly with the external magnetic field[132] according to $M = \chi_m \cdot B_0$, with χ_m the magnetic susceptibility of a material and B_0 the applied magnetic field strength (A/m). Since the severity of susceptibility artifacts increases with the magnetization of tissue, they also increase linearly with $\mathbf{B}_0$. Second, due to the T_2^* refocussing properties of the spin echo sequence, these are less affected by susceptibility artifacts compared to gradient echo sequences, which do not refocus T_2^* relaxation processes. This becomes especially clear in sequences incorporating EPI, which utilizes a train of gradient echoes for ultra-fast image acquisition (see Figure 1.18). Furthermore, utilization of longer TE will further escalate susceptibility artifacts for it provides more time for dephasing. Additionally, lower gradient strengths contribute to more pronounced susceptibility artifacts due to the mechanism by which spatial information is encoded by the frequency encoding gradient, as explained above for chemical shift displacement artifacts. Since magnetic susceptibility variations lead to localized changes in the Larmor frequency, MRI data reconstruction produces larger susceptibility artifacts at lower gradient strengths.

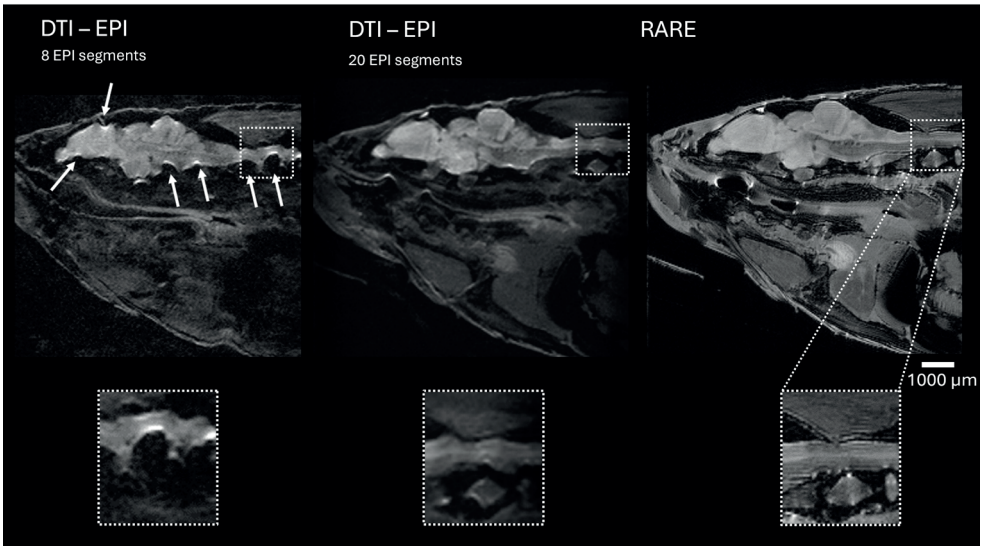

Figure 1.18 Susceptibility artifacts at UHF MRI (17.6 T / 750 MHz) *The first two images* ***[left & middle]*** *show DTI images each obtained with EPI, but at 8 and 20 segments, respectively. As the DTI image obtained with 8 EPI segments utilizes a longer gradient-echo train length, the susceptibility artifacts are more severe compared to the DTI image obtained with 20 EPI segment, although the susceptibility artifacts are still present. Contrary, the image obtained with a RARE MRI sequence shows very little susceptibility artifacts around the brain. From all three images, a zoomed image of the spinal cord is shown to highlight the severity of the susceptibility artifacts. All images were obtained with leptin deficient adult male zebrafish, at* $\boldsymbol{B}_0$ *17.6 T, Micro2.5 gradient system (Bruker Biospin GmbH, Germany)* G_{max} *= 1.5 T/m.*

4. MRI AND MRS OF THE ZEBRAFISH BRAIN

Although zebrafish are increasingly being used as an animal model for neurological disorders, the use of MRI or MRS to analyse the zebrafish brain is very limited compared to other model organisms (https://pubmed.ncbi.nlm.nih.gov/). The first report utilizing MRI to study anatomical structures in adult zebrafish, which included the zebrafish brain, was reported in 2006[125]. In 2010 the first high-resolution MRI images at 10 µm isotropic resolution of the zebrafish brain were reported[212]. This study utilized isolated zebrafish brains and employed contrast agents to enhance image quality for generating a three-dimensional digital atlas of the zebrafish brain[213]. In 2015, the same research group achieved another milestone by publishing the first whole-brain fibre tracking maps of the zebrafish brain through super-resolution track density imaging at 5 µm isotropic resolution, revealing intricate white matter structures in an isolated brain treated with contrast agents[192]. In 2023, Hamilton, Allen, and Reynolds conducted the first *in vivo* longitudinal examination of the zebrafish brain[214]. In addition, in 2009, the first and only known publication on performing localized MRS specifically on the zebrafish brain

was reported[65]. These advancements highlight the potential of MRI and MRS in zebrafish brain research, although technical challenges continue to limit their widespread application. These mainly arise from the tiny size of the zebrafish brain. As illustration in Table 1.3, the total volume of the zebrafish brain is approximately 4 mm^3, significantly smaller than the brain volume of other animal models or the human brain[213,215-225].

Obtaining high-resolution images of the zebrafish brain with good SNR within a reasonable measurement time, essential for visualizing and studying small structures, remains a challenge. It is well known that the SNR in MRI acquisition increases with the applied magnetic field strength[226], which can be leveraged to significantly reduce the required acquisition time needed to achieve the SNR[201]. To obtain near cellular resolution of 15 – 50 µm requires ultra-strong gradient systems. Strong gradients allow for superior encoding of spatial information, leading to the ability to distinguish smaller structures within the tissue. Since 1960, magnetic field strengths for MRI and MRS have increased almost linearly over the years (see Figure 1.19). Cellular level resolution (7 × 7 × 7 µm) in imaging of small biological structures has been demonstrated for visualizing individual bacteroids in root nodules[126]. In these experiments ultra-high magnetic field strength $\mathbf{B}_0$ = 22.3 T was used in combination with ultra-strong gradients (G_{max} = 3 T/m). By applying these advanced technologies to zebrafish brain imaging, we can potentially overcome many of the limitations posed by lower field strengths and gradient systems.

Table 1.3 *Comparison of average reported weight, volume, and number of neurons in the brain of humans, macaques, rats, mice, and zebrafish [213,215-225]. Created with biorender.com.*

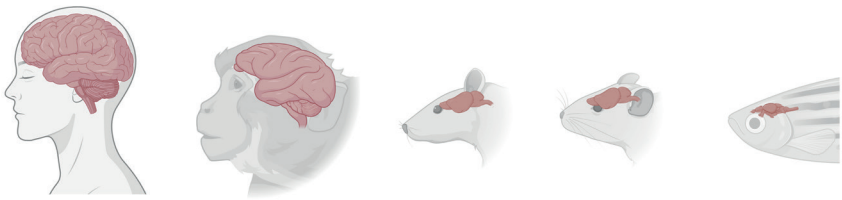

Species	Human (*Homo sapiens*)	Rhesus macaque (*Macaca mulatta*)	Rat (*Rattus*)	Mouse (*Mus musculus*)	Zebrafish (*Danio rerio*)
Brain weight (g)	1198 ♀ 1336 ♂	86.1 ♀ 96.1 ♂	1.8	0.4	0.001
Brain volume (mm^3)	$1130 \cdot 10^3$ ♀ $1260 \cdot 10^3$ ♂	$91.3 \cdot 10^3$ ♀ $98.7 \cdot 10^3$ ♂	1765	415	4
No. neurons	$86 \cdot 10^9$	$6.4 \cdot 10^9$	$200 \cdot 10^6$	$71 \cdot 10^6$	$10 \cdot 10^6$

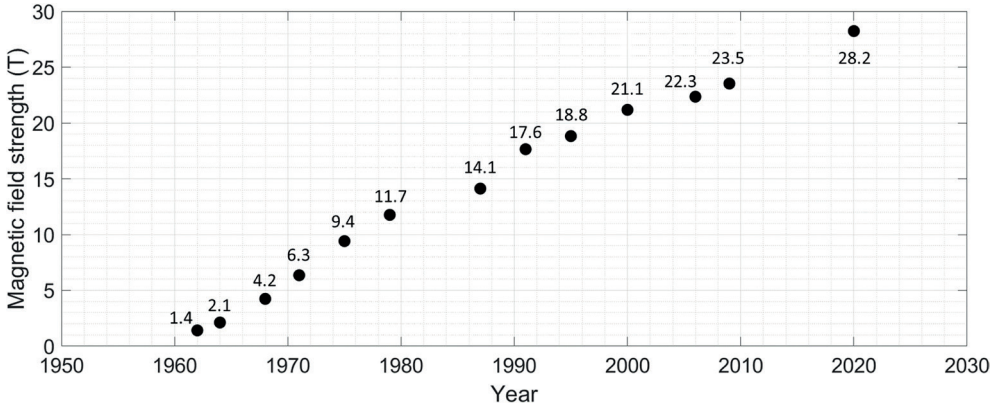

Figure 1.19 *Historical milestones of narrow bore (0.5 cm) magnetic field strength systems developed by Bruker Biospin GmbH, Germany. Data obtained from Bruker.*

5. THESIS SCOPE

In 2020, the introduction of technology operating at the highest commercially available magnetic field strength of 28.2 T marked the next historical milestone in the field of micro imaging. This UHF strength MRI system promises unparalleled spatial resolution and sensitivity, offering new opportunities for detailed anatomical and functional studies. This thesis aims to investigate the potential and challenges associated with using this advanced technology specifically for the examination of the zebrafish brain, an increasingly popular model organism in neurological research. The research presented in this work will focus on several key areas: conventional MRI for high-resolution anatomical imaging, dMRI for mapping the microstructural properties of neural tissues, and MRS for assessing the biochemical composition of the zebrafish brain. Each of these modalities will be evaluated for their efficacy in capturing the intricate details of zebrafish neuroanatomy and neurophysiology, which are critical for understanding fundamental biological processes and disease mechanisms. The ultra-high magnetic field strength of 28.2 T presents both opportunities and challenges. On the one hand, it enhances signal-to-noise ratio and spatial resolution, potentially allowing for unprecedented visualization of fine neural structures and subtle biochemical changes. On the other hand, it introduces technical challenges such as increased susceptibility and chemical shift artifacts. This thesis will systematically address these challenges, optimizing imaging protocols and developing strategies to mitigate artifacts and other issues.

In **Chapter 2**, various MRI and dMRI sequences are optimized for microstructural analysis of the zebrafish brain at exceptionally high spatial resolutions ranging from 23 to 50 µm. These optimizations are performed using the highest commercially available magnetic field strength of 28.2 T for imaging. Additionally, this chapter documents the first known instance of dMRI tractography of an intact zebrafish brain, employing advanced tractography algorithms to isolate white matter signals, thereby reducing noise. This enables the visualization and identification of tiny white matter structures at an extraordinary isotropic resolution of 5 µm.

Chapter 3 details the application of optimized MRI and dMRI techniques at 17.6 T to investigate microstructural changes resulting from toll-like receptor 2 (TLR2) deficiency in the zebrafish brain. In addition to analysing variations in the T_2 and *ADC* across different brain regions, advanced dMRI methods were employed. These included diffusion tensor imaging (DTI) and diffusion kurtosis imaging (DKI), which, alongside dMRI tractography, were used to specifically examine alterations in the integrity of small white matter structures in the zebrafish brain, revealing intriguing microstructural changes associated with compromised white matter integrity and axonal degeneration.

Chapter 4 describes the optimization of single voxel localized ^{1}H MRS at UHF MRI specifically for cerebral metabolic analysis in zebrafish. This chapter explores the potentials and challenges associated with UHF localized ^{1}H MRS on the zebrafish brain, with a focus on acquiring highly resolved spectra for targeted investigation of distinct brain regions. Highly resolved cerebral metabolite spectra were obtained from specific zebrafish brain regions, even from volumes as small as 125 nL. This enabled the identification and quantification of brain metabolites with exceptional resolution. Localized ^{1}H MRS at 28.2 T significantly enhanced the signal-to-noise ratio and improved the baseline separation of metabolite signals from these localized regions in the tiny zebrafish brain. This advancement extends the available techniques for utilizing zebrafish in neurological disorder research.

In **Chapter 5**, we delve into the cerebral metabolic changes occurring in the zebrafish brain as a direct consequence of TLR2 deficiency. This study employs a sophisticated combination of high-resolution magic angle spinning (HR-MAS) at 14.1 T to conduct whole-brain analysis and localized ^{1}H MRS at 28.2 T to focus on specific brain regions. Through these advanced techniques, we observed significant alterations in the levels of various neurotransmitters and metabolites that play critical roles in cerebral energy homeostasis. Notably, there was a substantial increase in lactate levels, which may be indicative of an elevated energy demand within the brain. Furthermore, we link the observed metabolic changes to previous findings to propose a model describing the effect of toll-like receptor 2 deficiency on the brain's microstructure.

Finally, **Chapter 6** presents a comprehensive discussion of the work presented in this thesis, offers a future outlook, and includes initial results of MRI and dMRI for other pathological zebrafish models. In this chapter I also provide suggestions of how the presented methods may be applied or modified for *in vivo* applications.

REFERENCES

1 G. B. D. Nervous System Disorders Collaborators, Global, regional, and national burden of disorders affecting the nervous system, 1990-2021: a systematic analysis for the Global Burden of Disease Study 2021. *Lancet Neurol* **23**, 344-381 (2024). https://doi.org/10.1016/S1474-4422(24)00038-3

2 Gooch, C. L., Pracht, E. & Borenstein, A. R. The burden of neurological disease in the United States: A summary report and call to action. *Ann Neurol* **81**, 479-484 (2017). https://doi.org/10.1002/ana.24897

3 Olesen, J. The cost of neurological disorders in Europe. *Public policy and health economics* **357** (2015). https://doi.org/https://doi.org/10.1016/j.jns.2015.09.303

4 Prince, M. *et al. World Alzheimer Report 2015. The Global Impact of Dementia. An Analysis of Prevalence, Incidence, Cost and Trends*. (2015).

5 Bovenkerk, B. & Kaldewaij, F. The use of animal models in behavioural neuroscience research. *Curr Top Behav Neurosci* **19**, 17-46 (2015). https://doi.org/10.1007/7854_2014_329

6 Montanari, M., Bonsi, P., Martella, G. & Wirz, A. Animal Models in Neuroscience: What Is the "Culture of Care"? *Encyclopedia* **4**, 215-233 (2024).

7 Attfield, K. E., Jensen, L. T., Kaufmann, M., Friese, M. A. & Fugger, L. The immunology of multiple sclerosis. *Nature Reviews Immunology* **22**, 734-750 (2022). https://doi.org/10.1038/s41577-022-00718-z

8 Jevtic, S., Sengar, A. S., Salter, M. W. & McLaurin, J. The role of the immune system in Alzheimer disease: Etiology and treatment. *Ageing Research Reviews* **40**, 84-94 (2017). https://doi.org/https://doi.org/10.1016/j.arr.2017.08.005

9 Tansey, M. G. & Romero-Ramos, M. Immune system responses in Parkinson's disease: Early and dynamic. *Eur J Neurosci* **49**, 364-383 (2019). https://doi.org/10.1111/ejn.14290

10 Bonilla, F. A. & Oettgen, H. C. Adaptive immunity. *Journal of Allergy and Clinical Immunology* **125**, S33-S40 (2010). https://doi.org/https://doi.org/10.1016/j.jaci.2009.09.017

11 Akira, S., Uematsu, S. & Takeuchi, O. Pathogen recognition and innate immunity. *Cell* **124**, 783-801 (2006). https://doi.org/10.1016/j.cell.2006.02.015

12 Hanke, M. L. & Kielian, T. Toll-like receptors in health and disease in the brain: mechanisms and therapeutic potential. *Clin Sci (Lond)* **121**, 367-387 (2011). https://doi.org/10.1042/cs20110164

13 Beg, A. A. Endogenous ligands of Toll-like receptors: implications for regulating inflammatory and immune responses. *Trends Immunol* **23**, 509-512 (2002). https://doi.org/10.1016/s1471-4906(02)02317-7

14 Matzinger, P. The danger model: a renewed sense of self. *Science* **296**, 301-305 (2002). https://doi.org/10.1126/science.1071059

15 Hu, W. & Spaink, H. P. The Role of TLR2 in Infectious Diseases Caused by Mycobacteria: From Cell Biology to Therapeutic Target. *Biology (Basel)* **11** (2022). https://doi.org/10.3390/biology11020246

16 Jin, M. S. & Lee, J.-O. Structures of the toll-like receptor family and its ligand complexes. *Immunity* **29**, 182-191 (2008).

17 Behzadi, P., Garcia-Perdomo, H. A. & Karpinski, T. M. Toll-Like Receptors: General Molecular and Structural Biology. *J Immunol Res* **2021**, 9914854 (2021). https://doi.org/10.1155/2021/9914854

18 Kornilov, F. D. *et al.* The architecture of transmembrane and cytoplasmic juxtamembrane regions of Toll-like receptors. *Nature Communications* **14**, 1503 (2023). https://doi.org/10.1038/s41467-023-37042-6

19 Takeuchi, O. & Akira, S. Pattern recognition receptors and inflammation. *Cell* **140**, 805-820 (2010). https://doi.org/10.1016/j.cell.2010.01.022

20 Kawagoe, T. *et al.* Sequential control of Toll-like receptor-dependent responses by IRAK1 and IRAK2. *Nat Immunol* **9**, 684-691 (2008). https://doi.org/10.1038/ni.1606

21 Xia, Z. P. *et al.* Direct activation of protein kinases by unanchored polyubiquitin chains. *Nature* **461**, 114-119 (2009). https://doi.org/10.1038/nature08247

22 Meijer, A. H. *et al.* Expression analysis of the Toll-like receptor and TIR domain adaptor families of zebrafish. *Mol Immunol* **40**, 773-783 (2004). https://doi.org/10.1016/j.molimm.2003.10.003

23 Chen, H., Liang, Y., Han, Y., Liu, T. & Chen, S. Genome-wide analysis of Toll-like receptors in zebrafish and the effect of rearing temperature on the receptors in response to stimulated pathogen infection. *Journal of Fish Diseases* **44**, 337-349 (2021). https://doi.org/https://doi.org/10.1111/jfd.13287

24 Li, Y., Li, Y., Cao, X., Jin, X. & Jin, T. Pattern recognition receptors in zebrafish provide functional and evolutionary insight into innate immune signaling pathways. *Cell Mol Immunol* **14**, 80-89 (2017). https://doi.org/10.1038/cmi.2016.50

25 Acioglu, C., Heary, R. F. & Elkabes, S. Roles of neuronal toll-like receptors in neuropathic pain and central nervous system injuries and diseases. *Brain, Behavior, and Immunity* **102**, 163-178 (2022). https://doi.org/https://doi.org/10.1016/j.bbi.2022.02.016

26 Tuomanen, E., Liu, H., Hengstler, B., Zak, O. & Tomasz, A. The Induction of Meningeal Inflammation by Components of the Pneumococcal Cell Wall. *The Journal of Infectious Diseases* **151**, 859-868 (1985). https://doi.org/10.1093/infdis/151.5.859

27 Koedel, U., Scheld, W. M. & Pfister, H.-W. Pathogenesis and pathophysiology of pneumococcal meningitis. *The Lancet infectious diseases* **2**, 721-736 (2002).

28 Weber, J. R. & Tuomanen, E. I. Cellular damage in bacterial meningitis: an interplay of bacterial and host driven toxicity. *Journal of neuroimmunology* **184**, 45-52 (2007).

29 Momtazmanesh, S., Perry, G. & Rezaei, N. Toll-like receptors in Alzheimer's disease. *Journal of Neuroimmunology* **348**, 577362 (2020). https://doi.org/https://doi.org/10.1016/j.jneuroim.2020.577362

30 Kinney, J. W. *et al.* Inflammation as a central mechanism in Alzheimer's disease. *Alzheimer's & Dementia: Translational Research & Clinical Interventions* **4**, 575-590 (2018).

31 Gomez, W., Morales, R., Maracaja-Coutinho, V., Parra, V. & Nassif, M. Down syndrome and Alzheimer's disease: common molecular traits beyond the amyloid precursor protein. *Aging (Albany NY)* **12**, 1011 (2020).

32 Chakrabarty, P. *et al.* TLR5 decoy receptor as a novel anti-amyloid therapeutic for Alzheimer's disease. *Journal of Experimental Medicine* **215**, 2247-2264 (2018).

33 Walter, S. *et al.* Role of the toll-like receptor 4 in neuroinflammation in Alzheimer's disease. *Cellular Physiology and Biochemistry* **20**, 947-956 (2007).

34 Walker, D. G., Tang, T. M. & Lue, L.-F. Increased expression of toll-like receptor 3, an anti-viral signaling molecule, and related genes in Alzheimer's disease brains. *Experimental neurology* **309**, 91-106 (2018).

35 Gold, M. & El Khoury, J. in *Seminars in immunopathology*. 607-611 (Springer).

36 Frank, S., Copanaki, E., Burbach, G. J., Müller, U. C. & Deller, T. Differential regulation of toll-like receptor mRNAs in amyloid plaque-associated brain tissue of aged APP23 transgenic mice. *Neuroscience letters* **453**, 41-44 (2009).

37 Kiasalari, Z. *et al.* Ellagic acid ameliorates learning and memory deficits in a rat model of Alzheimer's disease: an exploration of underlying mechanisms. *Psychopharmacology* **234**, 1841-1852 (2017).

38 Rangasamy, S. B. *et al.* Selective disruption of TLR2-MyD88 interaction inhibits inflammation and attenuates Alzheimer's pathology. *The Journal of Clinical Investigation* **128**, 4297-4312 (2018).

39 Bsibsi, M., Ravid, R., Gveric, D. & van Noort, J. M. Broad expression of Toll-like receptors in the human central nervous system. *Journal of Neuropathology & Experimental Neurology* **61**, 1013-1021 (2002).

40 Go, M., Kou, J., Lim, J.-E., Yang, J. & Fukuchi, K.-i. Microglial response to LPS increases in wild-type mice during aging but diminishes in an Alzheimer's mouse model: implication of TLR4 signaling in disease progression. *Biochemical and biophysical research communications* **479**, 331-337 (2016).

41 Trotta, T., Porro, C., Calvello, R. & Panaro, M. A. Biological role of Toll-like receptor-4 in the brain. *Journal of neuroimmunology* **268**, 1-12 (2014).

42 Tahara, K. *et al.* Role of toll-like receptor signalling in Aβ uptake and clearance. *Brain* **129**, 3006-3019 (2006).

43 Pourbadie, H. G. *et al.* Early minor stimulation of microglial TLR2 and TLR4 receptors attenuates Alzheimer's disease–related cognitive deficit in rats: behavioral, molecular, and electrophysiological evidence. *Neurobiology of aging* **70**, 203-216 (2018).

44 Yousefi, N. *et al.* Prestimulation of microglia through TLR4 pathway promotes interferon beta expression in a rat model of Alzheimer's disease. *Journal of Molecular Neuroscience* **67**, 495-503 (2019).

45 Wu, L. *et al.* Toll-Like Receptor 4: A Promising Therapeutic Target for Alzheimer's Disease. *Mediators Inflamm* **2022**, 7924199 (2022). https://doi.org/10.1155/2022/7924199

46 Xiang, W., Chao, Z.-Y. & Feng, D.-Y. Role of Toll-like receptor/MYD88 signaling in neurodegenerative diseases. *Reviews in the neurosciences* **26**, 407-414 (2015).

47 Richard, K. L., Filali, M., Prefontaine, P. & Rivest, S. Toll-like receptor 2 acts as a natural innate immune receptor to clear amyloid beta 1-42 and delay the cognitive decline in a mouse model of Alzheimer's disease. *J Neurosci* **28**, 5784-5793 (2008). https://doi.org/10.1523/JNEUROSCI.1146-08.2008

48 Jana, M., Palencia, C. A. & Pahan, K. Fibrillar amyloid-β peptides activate microglia via TLR2: implications for Alzheimer's disease. *The Journal of Immunology* **181**, 7254-7262 (2008).

49 Zhou, C. *et al.* Genomic deletion of TLR2 induces aggravated white matter damage and deteriorated neurobehavioral functionsin mouse models of Alzheimer's disease. *Aging* **11** (2019). https://doi.org/10.18632/aging.102260

50 Allen, H. B. Alzheimer's disease: assessing the role of spirochetes, biofilms, the immune system, and amyloid-β with regard to potential treatment and prevention. *Journal of Alzheimer's Disease* **53**, 1271-1276 (2016).

51 Heidari, A., Yazdanpanah, N. & Rezaei, N. The role of Toll-like receptors and neuroinflammation in Parkinson's disease. *Journal of Neuroinflammation* **19**, 135 (2022). https://doi.org/10.1186/s12974-022-02496-w

52 Casula, M. *et al.* Toll-like receptor signaling in amyotrophic lateral sclerosis spinal cord tissue. *Neuroscience* **179**, 233-243 (2011). https://doi.org/10.1016/j.neuroscience.2011.02.001

53 Tajalli-Nezhad, S., Karimian, M., Beyer, C., Atlasi, M. A. & Azami Tameh, A. The regulatory role of Toll-like receptors after ischemic stroke: neurosteroids as TLR modulators with the focus on TLR2/4. *Cellular and Molecular Life Sciences* **76**, 523-537 (2019). https://doi.org/10.1007/s00018-018-2953-2

54 Hu W, Yang S, Shimada Y, Münch M, Marín-Juez R, Meijer AH, Spaink HP. Infection and RNA-seq analysis of a zebrafish tlr2 mutant shows a broad function of this toll-like receptor in transcriptional and metabolic control and defense to Mycobacterium marinum infection. BMC Genomics. 2019 Nov 20;20(1):878. doi: 10.1186/s12864-019-6265-1. PMID: 31747871; PMCID: PMC6869251.

55 Makałowski, W., Boguski, M., Hughes, A. & Yeager, M. Synonymous and nonsynonymous substitution distances are correlated in mouse and rat genes. *Journal of molecular evolution* **47**, 119-121 (1998).

56 Makałowski, W. & Boguski, M. S. Evolutionary parameters of the transcribed mammalian genome: an analysis of 2,820 orthologous rodent and human sequences. *Proceedings of the National Academy of Sciences* **95**, 9407-9412 (1998).

57 Lamerdin, J. E. *et al.* Genomic sequence comparison of the human and mouse XRCC1 DNA repair gene regions. *Genomics* **25**, 547-554 (1995).

58 Koop, B. F. & Hood, L. Striking sequence similarity over almost 100 kilobases of human and mouse T–cell receptor DNA. *Nature genetics* **7**, 48-53 (1994).

59 Giacomotto, J. & Ségalat, L. High-throughput screening and small animal models, where are we? *British Journal of Pharmacology* **160**, 204-216 (2010). https://doi.org/https://doi.org/10.1111/j.1476-5381.2010.00725.x

60 Streisinger, G., Walker, C., Dower, N., Knauber, D. & Singer, F. Production of clones of homozygous diploid zebra fish (Brachydanio rerio). *Nature* **291**, 293-296 (1981). https://doi.org/10.1038/291293a0

61 Mullins, M. C., Acedo, J. N., Priya, R., Solnica-Krezel, L. & Wilson, S. W. The zebrafish issue: 25 years on. *Development* **148** (2021). https://doi.org/10.1242/dev.200343

62 Sarasamma, S., Karim, A. & Orengo, J. P. Zebrafish Models of Rare Neurological Diseases like Spinocerebellar Ataxias (SCAs): Advantages and Limitations. *Biology* **12**, 1322 (2023).

63 Quiñonez-Silvero, C., Hübner, K. & Herzog, W. Development of the brain vasculature and the blood-brain barrier in zebrafish. *Dev Biol* **457**, 181-190 (2020). https://doi.org/10.1016/j.ydbio.2019.03.005

64 Lyons, D. A. & Talbot, W. S. Glial cell development and function in zebrafish. *Cold Spring Harb Perspect Biol* **7**, a020586 (2014). https://doi.org/10.1101/cshperspect.a020586

65 Kabli, S., Spaink, H. P., De Groot, H. J. & Alia, A. In vivo metabolite profile of adult zebrafish brain obtained by high-resolution localized magnetic resonance spectroscopy. *J Magn Reson Imaging* **29**, 275-281 (2009). https://doi.org/10.1002/jmri.21609

66 Braakman, N., Oerther, T., de Groot, H. J. & Alia, A. High resolution localized two-dimensional MR spectroscopy in mouse brain in vivo. *Magn Reson Med* **60**, 449-456 (2008). https://doi.org/10.1002/mrm.21662

67 Veeraiah, P. & Jansen, J. F. A. Multinuclear Magnetic Resonance Spectroscopy at Ultra-High-Field: Assessing Human Cerebral Metabolism in Healthy and Diseased States. *Metabolites* **13** (2023). https://doi.org/10.3390/metabo13040577

68 Fontana, B. D. *et al.* Zebrafish models for attention deficit hyperactivity disorder (ADHD). *Neurosci Biobehav Rev* **100**, 9-18 (2019). https://doi.org/10.1016/j.neubiorev.2019.02.009

69 Rea, V. & Van Raay, T. J. Using Zebrafish to Model Autism Spectrum Disorder: A Comparison of ASD Risk Genes Between Zebrafish and Their Mammalian Counterparts. *Frontiers in Molecular Neuroscience* **13** (2020). https://doi.org/10.3389/fnmol.2020.575575

70 Saleem, S. & Kannan, R. R. Zebrafish: an emerging real-time model system to study Alzheimer's disease and neurospecific drug discovery. *Cell Death Discov* **4**, 45 (2018). https://doi.org/10.1038/s41420-018-0109-7

71 Oliveira, N. A. S., Pinho, B. R. & Oliveira, J. M. A. Swimming against ALS: How to model disease in zebrafish for pathophysiological and behavioral studies. *Neurosci Biobehav Rev* **148**, 105138 (2023). https://doi.org/10.1016/j.neubiorev.2023.105138

72 Kumar, V., Singh, C. & Singh, A. Zebrafish an experimental model of Huntington's disease: molecular aspects, therapeutic targets and current challenges. *Mol Biol Rep* **48**, 8181-8194 (2021). https://doi.org/10.1007/s11033-021-06787-y

73 Doyle, J. M. & Croll, R. P. A Critical Review of Zebrafish Models of Parkinson's Disease. *Front Pharmacol* **13**, 835827 (2022). https://doi.org/10.3389/fphar.2022.835827

74 Chen, W. *et al.* Zebrafish as a Model for In-Depth Mechanistic Study for Stroke. *Transl Stroke Res* **12**, 695-710 (2021). https://doi.org/10.1007/s12975-021-00907-3

75 Walcott, B. P. & Peterson, R. T. Zebrafish models of cerebrovascular disease. *J Cereb Blood Flow Metab* **34**, 571-577 (2014). https://doi.org/10.1038/jcbfm.2014.27

76 D'Amora, M. *et al.* Zebrafish as an Innovative Tool for Epilepsy Modeling: State of the Art and Potential Future Directions. *Int J Mol Sci* **24** (2023). https://doi.org/10.3390/ijms24097702

77 Kulkarni, P. *et al.* Novel Zebrafish EAE model: A quick in vivo screen for multiple sclerosis. *Multiple Sclerosis and Related Disorders* **11**, 32-39 (2017). https://doi.org/https://doi.org/10.1016/j.msard.2016.11.010

78 Richert, E. *Zebrafish Model of Schizophrenia*, (2021).

79 Tikhonova, M. A. *et al.* A Novel Laser-Based Zebrafish Model for Studying Traumatic Brain Injury and Its Molecular Targets. *Pharmaceutics* **14** (2022). https://doi.org/10.3390/pharmaceutics14081751

80 Reimunde, P. *et al.* Cellular and Molecular Mechanisms Underlying Glioblastoma and Zebrafish Models for the Discovery of New Treatments. *Cancers (Basel)* **13** (2021). https://doi.org/10.3390/cancers13051087

81 Hu, W. *et al.* Transcriptomic and Metabolomic Studies Reveal That Toll-like Receptor 2 Has a Role in Glucose-Related Metabolism in Unchallenged Zebrafish Larvae (Danio rerio). *Biology (Basel)* **12** (2023). https://doi.org/10.3390/biology12020323

82 Martucci, M. *et al.* Magnetic Resonance Imaging of Primary Adult Brain Tumors: State of the Art and Future Perspectives. *Biomedicines* **11** (2023). https://doi.org/10.3390/biomedicines11020364

83 Rangarajan, K., Das, C. J., Kumar, A. & Gupta, A. K. MRI in central nervous system infections: A simplified patterned approach. *World J Radiol* **6**, 716-725 (2014). https://doi.org/10.4329/wjr.v6.i9.716

84 Lee, H., Yang, Y., Xu, J., Ware, J. B. & Liu, B. Use of Magnetic Resonance Imaging in Acute Traumatic Brain Injury Patients is Associated with Lower Inpatient Mortality. *J Clin Imaging Sci* **11**, 53 (2021). https://doi.org/10.25259/jcis_148_2021

85 Tedyanto, E. H., Tini, K. & Pramana, N. A. K. Magnetic Resonance Imaging in Acute Ischemic Stroke. *Cureus* **14**, e27224 (2022). https://doi.org/10.7759/cureus.27224

86 Kartal, M. G. & Algin, O. Evaluation of hydrocephalus and other cerebrospinal fluid disorders with MRI: An update. *Insights Imaging* **5**, 531-541 (2014). https://doi.org/10.1007/s13244-014-0333-5

87 Heit, J. J., Iv, M. & Wintermark, M. Imaging of Intracranial Hemorrhage. *J Stroke* **19**, 11-27 (2017). https://doi.org/10.5853/jos.2016.00563

88 Sharma, U. & Jagannathan, N. R. Metabolism of prostate cancer by magnetic resonance spectroscopy (MRS). *Biophys Rev* **12**, 1163-1173 (2020). https://doi.org/10.1007/s12551-020-00758-6

89 Cowin, G. J. *et al.* Magnetic resonance imaging and spectroscopy for monitoring liver steatosis. *J Magn Reson Imaging* **28**, 937-945 (2008). https://doi.org/10.1002/jmri.21542

90 Ali, H. A. *et al.* Predictive Value of In Vivo MR Spectroscopy With Semilocalization by Adiabatic Selective Refocusing in Differentiating Clear Cell Renal Cell Carcinoma From Other Subtypes. *AJR Am J Roentgenol* **214**, 817-824 (2020). https://doi.org/10.2214/AJR.19.22023

91 Brown, J. J., Mirowitz, S. A., Sandstrom, J. C. & Perman, W. H. MR Spectroscopy of the heart. *American Journal of Roentgenology* **155** (1990).

92 Graff-Radford, J. & Kantarci, K. Magnetic resonance spectroscopy in Alzheimer's disease. *Neuropsychiatr Dis Treat* **9**, 687-696 (2013). https://doi.org/10.2147/NDT.S35440

93 Weinberg, B. D., Kuruva, M., Shim, H. & Mullins, M. E. Clinical Applications of Magnetic Resonance Spectroscopy in Brain Tumors: From Diagnosis to Treatment. *Radiol Clin North Am* **59**, 349-362 (2021). https://doi.org/10.1016/j.rcl.2021.01.004

94 Nakahara, T. *et al.* Glutamatergic and GABAergic metabolite levels in schizophrenia-spectrum disorders: a meta-analysis of (1)H-magnetic resonance spectroscopy studies. *Mol Psychiatry* **27**, 744-757 (2022). https://doi.org/10.1038/s41380-021-01297-6

95 Kalra, S. Magnetic Resonance Spectroscopy in ALS. *Front Neurol* **10**, 482 (2019). https://doi.org/10.3389/fneur.2019.00482

96 Pan, J. W. & Kuzniecky, R. I. Utility of magnetic resonance spectroscopic imaging for human epilepsy. *Quant Imaging Med Surg* **5**, 313-322 (2015). https://doi.org/10.3978/j.issn.2223-4292.2015.01.03

97 Sajja, B. R., Wolinsky, J. S. & Narayana, P. A. Proton magnetic resonance spectroscopy in multiple sclerosis. *Neuroimaging Clin N Am* **19**, 45-58 (2009). https://doi.org/10.1016/j.nic.2008.08.002

98 Shoeibi, A. *et al.* Brain proton magnetic resonance spectroscopy in patients with Parkinson's disease. *Curr J Neurol* **21**, 156-161 (2022). https://doi.org/10.18502/cjn.v21i3.11108

99 Eeza, M. N. H. *et al.* Metabolic Profiling of Suprachiasmatic Nucleus Reveals Multifaceted Effects in an Alzheimer's Disease Mouse Model. *J Alzheimers Dis* (2021). https://doi.org/10.3233/JAD-201575

100 Miller, B. L. *et al.* Alzheimer disease: depiction of increased cerebral myo-inositol with proton MR spectroscopy. *Radiology* **187**, 4 (1993). https://doi.org/10.1148/radiology.187.2.8475286.

101 Bitsch, A. *et al.* Inflammatory CNS demyelination: histopathologic correlation with in vivo quantitative proton MR spectroscopy. *Am J Neuroradiol* **9**, 1619-1627 (1999).

102 Mader, I., Rauer, S., Gall, P. & Klose, U. (1)H MR spectroscopy of inflammation, infection and ischemia of the brain. *Eur J Radiol* **67**, 250-257 (2008). https://doi.org/10.1016/j.ejrad.2008.02.033

103 Young, S. P. *et al.* The impact of inflammation on metabolomic profiles in patients with arthritis. *Arthritis Rheum* **65**, 2015-2023 (2013). https://doi.org/10.1002/art.38021

104 Cocco, E. *et al.* (1)H-NMR analysis provides a metabolomic profile of patients with multiple sclerosis. *Neurol Neuroimmunol Neuroinflamm* **3**, 1-9 (2016). https://doi.org/10.1212/NXI.0000000000000185

105 Kim, H. H. *et al.* Metabolomic profiling of CSF in multiple sclerosis and neuromyelitis optica spectrum disorder by nuclear magnetic resonance. *PLoS One* **12**, 21 (2017). https://doi.org/10.1371/journal.pone.0181758

106 Battini, S. *et al.* Metabolomics approaches in experimental allergic encephalomyelitis. *J Neuroimmunol* **314**, 94-100 (2018). https://doi.org/10.1016/j.jneuroim.2017.11.018

107 French, C. D. *et al.* NMR metabolomics of cerebrospinal fluid differentiates inflammatory diseases of the central nervous system. *PLOS Negl Trop Dis* **12**, 1-17 (2018). https://doi.org/10.1371/journal.pntd.0007045

108 Fernando, K. T. *et al.* Elevated white matter myo-inositol in clinically isolated syndromes suggestive of multiple sclerosis. *Brain* **127**, 1361-1369 (2004). https://doi.org/10.1093/brain/awh153

109 Kazama, M. *et al.* Astrocytes release glutamate via cystine/glutamate antiporter upregulated in response to increased oxidative stress related to sporadic amyotrophic lateral sclerosis. *Neuropathology* **40**, 587-598 (2020). https://doi.org/10.1111/neup.12716

110 Iovino, L., Tremblay, M. E. & Civiero, L. Glutamate-induced excitotoxicity in Parkinson's disease: The role of glial cells. *J Pharmacol Sci* **144**, 151-164 (2020). https://doi.org/10.1016/j.jphs.2020.07.011

111 Maszka, P. *et al.* Metabolomic Footprint of Disrupted Energetics and Amino Acid Metabolism in Neurodegenerative Diseases: Perspectives for Early Diagnosis and Monitoring of Therapy. *Metabolites* **13** (2023). https://doi.org/10.3390/metabo13030369

112 Bloch, F., Hansen, W. W. & Packard, M. The Nuclear Induction Experiment. *Physical Review* **70**, 474-485 (1946). https://doi.org/10.1103/PhysRev.70.474

113 Purcell, E. M., Torrey, H. C. & Pound, R. V. Resonance Absorption by Nuclear Magnetic Moments in a Solid. *Physical Review* **69**, 37-38 (1946). https://doi.org/10.1103/PhysRev.69.37

114 *The Nobel Prize in Physics 1952*, <https://www.nobelprize.org/prizes/physics/1952/summary> (

115 Friebolin, H. *Basic One- and Two-Dimensional NMR Spectroscopy, 5th, Completely Revised and Updated Edition*. 442 (Wiley-VCH, 2010).

116 Wielpütz, M. & Kauczor, H.-U. MRI of the lung: state of the art. Diagnostic and interventional radiology 18, 344 (2012).

117 Bertoli, D. et al. A novel MRI-based three-dimensional model of stomach volume, surface area, and geometry in response to gastric filling and emptying. Neurogastroenterology & Motility 35, e14497 (2023). https://doi.org/https://doi.org/10.1111/nmo.14497

118 Feinberg, D. A. *et al.* Next-generation MRI scanner designed for ultra-high-resolution human brain imaging at 7 Tesla. *Nat Methods* **20**, 2048-2057 (2023). https://doi.org/10.1038/s41592-023-02068-7

119 Menon, R. G., Chang, G. & Regatte, R. R. Musculoskeletal MR Imaging Applications at Ultra-High (7T) Field Strength. *Magn Reson Imaging Clin N Am* **29**, 117-127 (2021). https://doi.org/10.1016/j.mric.2020.09.008

120 Umutlu, L. *et al.* Contrast-enhanced ultra-high-field liver MRI: a feasibility trial. *Eur J Radiol* **82**, 760-767 (2013). https://doi.org/10.1016/j.ejrad.2011.07.004

121 Kataoka, M. *et al.* Ultrafast Dynamic Contrast-enhanced MRI of the Breast: How Is It Used? *Magn Reson Med Sci* **21**, 83-94 (2022). https://doi.org/10.2463/mrms.rev.2021-0157

122 Nikken, J. J. & Krestin, G. P. MRI of the kidney-state of the art. *Eur Radiol* **17**, 2780-2793 (2007). https://doi.org/10.1007/s00330-007-0701-3

123 Schreiber, L. M. *et al.* Ultra-high field cardiac MRI in large animals and humans for translational cardiovascular research. *Front Cardiovasc Med* **10**, 1068390 (2023). https://doi.org/10.3389/fcvm.2023.1068390

124 Braakman, N. *et al.* Longitudinal assessment of Alzheimer's beta-amyloid plaque development in transgenic mice monitored by in vivo magnetic resonance microimaging. *J Magn Reson Imaging* **24**, 530-536 (2006). https://doi.org/10.1002/jmri.20675

125 Kabli, S., Alia, A., Spaink, H. P., Verbeek, F. J. & De Groot, H. J. Magnetic resonance microscopy of the adult zebrafish. *Zebrafish* **3**, 431-439 (2006). https://doi.org/10.1089/zeb.2006.3.431

126 van Schadewijk, R. *et al.* Magnetic Resonance Microscopy at Cellular Resolution and Localised Spectroscopy of Medicago truncatula at 22.3 Tesla. *Sci Rep* **10**, 971 (2020). https://doi.org/10.1038/s41598-020-57861-7

127 Hahn, E. L. Spin Echoes. *Physical Review* **80**, 580-594 (1950). https://doi.org/10.1103/PhysRev.80.580

128 Hennig, J., Nauerth, A. & Friedburg, H. RARE Imaging: A Fast Imaging Method for Clinical MR *Magnetic Resonance in Medicine* **3**, 11 (1986). https://doi.org/https://doi.org/10.1002/mrm.1910030602

129 Kara, F. *et al.* In vivo measurement of transverse relaxation time in the mouse brain at 17.6 T. *Magn Reson Med* **70**, 985-993 (2013). https://doi.org/10.1002/mrm.24533

130 de Graaf, R. A. *et al.* High magnetic field water and metabolite proton T1 and T2 relaxation in rat brain in vivo. *Magn Reson Med* **56**, 386-394 (2006). https://doi.org/10.1002/mrm.20946

131 Lee, M. J. *et al.* Overcoming Artifacts from Metallic Orthopedic Implants at High-Field-Strength MR Imaging and Multi-detector CT1. *Radiographics* **27**, 13 (2007). https://doi.org/10.1148/rg.273065087

132 Lüdeke, K., Röschmann, P. & Tischler, R. Susceptibility artefacts in NMR imaging. *Magnetic Resonance Imaging* **3**, 15 (1985).

133 Hardy, P. A., Henkelman, R. M., Bishop, J. E., Poon, E. C. S. & Plewes, D. B. Why fat is bright in rare and fast spin-echo imaging. *Journal of magnetic Resonance Imaging* **2**, 8 (1992).

134 Poustchi-Amin, M., Mirowitz, S. A., Brown, J. J., McKinstry, R. C. & Li, T. Principles and Applications of Echo-planar Imaging: A Review for the General Radiologist. *RadioGraphics* **21**, 767-779 (2001). https://doi.org/10.1148/radiographics.21.3.g01ma23767

135 Bottomley, P. A., Foster, T. H., Argersinger, R. E. & Pfeifer, L. M. A review of normal tissue hydrogen NMR relaxation times and relaxation mechanisms from 1-100 MHz: dependence on tissue type, NMR frequency, temperature, species, excision, and age. *Med Phys* **11**, 425-448 (1984). https://doi.org/10.1118/1.595535

136 Abd-Ellah, M. K., Awad, A. I., Khalaf, A. A. M. & Hamed, H. F. A. A review on brain tumor diagnosis from MRI images: Practical implications, key achievements, and lessons learned. *Magn Reson Imaging* **61**, 300-318 (2019). https://doi.org/10.1016/j.mri.2019.05.028

137 Harms, S. E., Siemers, P. T., Hildenbrand, P. & Plum, G. Multiple spin echo magnetic resonance imaging of the brain. *RadioGraphics* **6**, 117-134 (1986). https://doi.org/10.1148/radiographics.6.1.3685481

138 Carr, H. Y. & Purcell, E. M. Effects of Diffusion on Free Precession in Nuclear Magnetic Resonance Experiments. *Physical Review* **94**, 630-638 (1954). https://doi.org/10.1103/PhysRev.94.630

139 Milford, D., Rosbach, N., Bendszus, M. & Heiland, S. Mono-Exponential Fitting in T2-Relaxometry: Relevance of Offset and First Echo. *PLoS One* **10**, e0145255 (2015). https://doi.org/10.1371/journal.pone.0145255

140 Majumdar, S., Orphanoudakis, S. C., Gmitro, A., O'Donnell, M. & Gore, J. C. Errors in the measurements of T2 using multiple-echo MRI techniques. I. Effects of radiofrequency pulse imperfections. *Magn Reson Med* **3**, 397-417 (1986). https://doi.org/10.1002/mrm.1910030305

141 Zelaya, F. O. *et al.* Direct visualisation of B1 inhomogeneity by flip angle dependency. *Magn Reson Imaging* **15**, 497-504 (1997). https://doi.org/10.1016/s0730-725x(96)00396-7

142 Dietrich, O., Reiser, M. F. & Schoenberg, S. O. Artifacts in 3-T MRI: physical background and reduction strategies. *Eur J Radiol* **65**, 29-35 (2008). https://doi.org/10.1016/j.ejrad.2007.11.005

143 Einstein, A. Über die von der molekularkinetischen Theorie der Wärme geforderte Bewegung von in ruhenden Flüssigkeiten suspendierten Teilchen. *Annalen der Physik* **322**, 549-560 (1905). https://doi.org/ https://doi.org/10.1002/andp.19053220806

144 Campbell, J. S. W. & Bruce Pike, G. in *Encyclopedia of Biomedical Engineering* (ed Roger Narayan) 505-518 (Elsevier, 2019).

145 Messina, C. *et al.* Diffusion-Weighted Imaging in Oncology: An Update. *Cancers* **12**, 1493 (2020).

146 Guirguis, M., Sharan, G., Wang, J. & Chhabra, A. Diffusion-weighted MR imaging of musculoskeletal tissues: incremental role over conventional MR imaging in bone, soft tissue, and nerve lesions. *BJR|Open* **4** (2022). https://doi.org/10.1259/bjro.20210077

147 Mekkaoui, C., Reese, T. G., Jackowski, M. P., Bhat, H. & Sosnovik, D. E. Diffusion MRI in the heart. *NMR in Biomedicine* **30**, e3426 (2017). https://doi.org/https://doi.org/10.1002/nbm.3426

148 Srinivasan, A., Goyal, M., Azri, F. A. & Lum, C. State-of-the-Art Imaging of Acute Stroke. *RadioGraphics* **26**, S75-S95 (2006). https://doi.org/10.1148/rg.26si065501

149 Bollineni, V. R., Kramer, G., Liu, Y., Melidis, C. & deSouza, N. M. A literature review of the association between diffusion-weighted MRI derived apparent diffusion coefficient and tumour aggressiveness in pelvic cancer. *Cancer Treatment Reviews* **41**, 496-502 (2015). https://doi.org/10.1016/j.ctrv.2015.03.010

150 Nalaini, F., Shahbazi, F., Mousavinezhad, S. M., Ansari, A. & Salehi, M. Diagnostic accuracy of apparent diffusion coefficient (ADC) value in differentiating malignant from benign solid liver lesions: a systematic review and meta-analysis. *British Journal of Radiology* **94** (2021). https://doi.org/10.1259/bjr.20210059

151 Vollenbrock, S. E., Voncken, F. E. M., Bartels, L. W., Beets-Tan, R. G. H. & Bartels-Rutten, A. Diffusion-weighted MRI with ADC mapping for response prediction and assessment of oesophageal cancer: A systematic review. *Radiotherapy and Oncology* **142**, 17-26 (2020). https://doi.org/10.1016/j.radonc.2019.07.006

152 Trivedi, R., Rathore, R. K. S. & Gupta, R. K. Review: Clinical application of diffusion tensor imaging. *Indian J Radiol Imaging* **18**, 7 (2008). https://doi.org/10.4103/0971-3026.38505

153 Steven, A. J., Zhuo, J. & Melhem, E. R. Diffusion Kurtosis Imaging: An Emerging Technique for Evaluating the Microstructural Environment of the Brain. *American Journal of Roentgenology* **202**, W26-W33 (2014). https://doi.org/10.2214/ajr.13.11365

154 Harkins, K. D., Beaulieu, C., Xu, J., Gore, J. C. & Does, M. D. A simple estimate of axon size with diffusion MRI. *NeuroImage* **227**, 117619 (2021). https://doi.org/https://doi.org/10.1016/j.neuroimage.2020.117619

155 Zhang, F. *et al.* Quantitative mapping of the brain's structural connectivity using diffusion MRI tractography: A review. *NeuroImage* **249**, 118870 (2022). https://doi.org/https://doi.org/10.1016/j.neuroimage.2021.118870

156 Bihan, D. L. *et al.* MR imaging of intravoxel incoherent motions: application to diffusion and perfusion in neurologic disorders. *Radiology* **161**, 401-407 (1986). https://doi.org/10.1148/radiology.161.2.3763909

157 Baliyan, V., Das, C. J., Sharma, R. & Gupta, A. K. Diffusion weighted imaging: Technique and applications. *World J Radiol* **8**, 785-798 (2016). https://doi.org/10.4329/wjr.v8.i9.785

158 Heemskerk, A. M. & Damon, B. M. Diffusion Tensor MRI Assessment of Skeletal Muscle Architecture. *Curr Med Imaging Rev* **3**, 152-160 (2007). https://doi.org/10.2174/157340507781386988

159 Serai, S. D. *et al.* Diffusion tensor imaging of the kidney in healthy controls and in children and young adults with autosomal recessive polycystic kidney disease. *Abdominal Radiology* **44**, 1867-1872 (2019). https://doi.org/10.1007/s00261-019-01933-4

160 Lee, Y. & Kim, H. Assessment of diffusion tensor MR imaging (DTI) in liver fibrosis with minimal confounding effect of hepatic steatosis. *Magnetic Resonance in Medicine* **73**, 1602-1608 (2015). https://doi.org/https://doi.org/10.1002/mrm.25253

161 Vedantam, A. *et al.* Diffusion Tensor Imaging of the Spinal Cord: Insights From Animal and Human Studies. *Neurosurgery* **74** (2014).

162 O'Donnell, L. J. & Westin, C.-F. An Introduction to Diffusion Tensor Image Analysis. *Neurosurgery Clinics of North America* **22**, 185-196 (2011). https://doi.org/https://doi.org/10.1016/j.nec.2010.12.004

163 Alexander, A. L., Lee, J. E., Lazar, M. & Field, A. S. Diffusion tensor imaging of the brain. *Neurotherapeutics* **4**, 316-329 (2007). https://doi.org/10.1016/j.nurt.2007.05.011

164 Skare, S., Hedehus, M., Moseley, M. E. & Li, T.-Q. Condition Number as a Measure of Noise Performance of Diffusion Tensor Data Acquisition Schemes with MRI. *Journal of Magnetic Resonance* **147**, 340-352 (2000). https://doi.org/https://doi.org/10.1006/jmre.2000.2209

165 in *Studies in Mathematics and Its Applications* Vol. 28 (ed G. Meurant) 1-68 (Elsevier, 1999).

166 Lo Buono, V. *et al.* Diffusion tensor imaging of white matter degeneration in early stage of Alzheimer's disease: a review. *International Journal of Neuroscience* **130**, 243-250 (2020). https://doi.org/10.1080/00207454.2019.1667798

167 Estevez-Fraga, C., Scahill, R., Rees, G., Tabrizi, S. J. & Gregory, S. Diffusion imaging in Huntington's disease: comprehensive review. *Journal of Neurology, Neurosurgery & Psychiatry* **92**, 62-69 (2021). https://doi.org/10.1136/jnnp-2020-324377

168 Zhang, Y. & Burock, M. A. Diffusion Tensor Imaging in Parkinson's Disease and Parkinsonian Syndrome: A Systematic Review. *Front Neurol* **11**, 531993 (2020). https://doi.org/10.3389/fneur.2020.531993

169 Christidi, F. *et al.* Diffusion Tensor Imaging as a Prognostic Tool for Recovery in Acute and Hyperacute Stroke. *Neurology International* **14**, 841-874 (2022).

170 Davanian, F., Faeghi, F., Shahzadi, S. & Farshidfar, Z. Evaluation of Diffusion Anisotropy and Diffusion Shape in Grading of Glial Tumors. *J Biomed Phys Eng* **9**, 459-464 (2019). https://doi.org/10.31661/jbpe.v0i0.513

171 Parlatini, V. *et al.* White matter alterations in Attention-Deficit/Hyperactivity Disorder (ADHD): a systematic review of 129 diffusion imaging studies with meta-analysis. *Molecular Psychiatry* **28**, 4098-4123 (2023). https://doi.org/10.1038/s41380-023-02173-1

172 Song, S.-K. *et al.* Dysmyelination Revealed through MRI as Increased Radial (but Unchanged Axial) Diffusion of Water. *NeuroImage* **17**, 1429-1436 (2002). https://doi.org/https://doi.org/10.1006/nimg.2002.1267

173 Winklewski, P. J. *et al.* Understanding the Physiopathology Behind Axial and Radial Diffusivity Changes-What Do We Know? *Front Neurol* **9**, 92 (2018). https://doi.org/10.3389/fneur.2018.00092

174 Figley, C. R. *et al.* Potential Pitfalls of Using Fractional Anisotropy, Axial Diffusivity, and Radial Diffusivity as Biomarkers of Cerebral White Matter Microstructure. *Front Neurosci* **15**, 799576 (2021). https://doi.org/10.3389/fnins.2021.799576

175 Steven, A. J., Zhuo, J. & Melhem, E. R. Diffusion kurtosis imaging: an emerging technique for evaluating the microstructural environment of the brain. *AJR Am J Roentgenol* **202**, W26-33 (2014). https://doi.org/10.2214/AJR.13.11365

176 Collier, Q. *Robust estimation of diffusion tensor and diffusion kurtosis imagingparameters* PhD thesis, Universiteit Antwerpen, (2018).

177 Jensen, J. H., Helpern, J. A., Ramani, A., Lu, H. & Kaczynski, K. Diffusional kurtosis imaging: the quantification of non-gaussian water diffusion by means of magnetic resonance imaging. *Magn Reson Med* **53**, 1432-1440 (2005). https://doi.org/10.1002/mrm.20508

178 Veraart, J., Sijbers, J., Sunaert, S., Leemans, A. & Jeurissen, B. Weighted linear least squares estimation of diffusion MRI parameters: strengths, limitations, and pitfalls. *Neuroimage* **81**, 335-346 (2013). https://doi.org/10.1016/j.neuroimage.2013.05.028

179 Boucher, S. *et al.* Diffusion Tensor Imaging Tractography of White Matter Tracts in the Equine Brain. *Frontiers in Veterinary Science* **7** (2020). https://doi.org/10.3389/fvets.2020.00382

180 Yeh, F.-C., Irimia, A., Bastos, D. C. d. A. & Golby, A. J. Tractography methods and findings in brain tumors and traumatic brain injury. *NeuroImage* **245**, 118651 (2021). https://doi.org/https://doi.org/10.1016/j.neuroimage.2021.118651

181 Soni, N., Mehrotra, A., Behari, S., Kumar, S. & Gupta, N. Diffusion-tensor Imaging and Tractography Application in Pre-operative Planning of Intra-axial Brain Lesions. *Cureus* **9**, e1739 (2017). https://doi.org/10.7759/cureus.1739

182 Abhinav, K. *et al.* Advanced diffusion MRI fiber tracking in neurosurgical and neurodegenerative disorders and neuroanatomical studies: A review. *Biochimica et Biophysica Acta (BBA) - Molecular Basis of Disease* **1842**, 2286-2297 (2014). https://doi.org/https://doi.org/10.1016/j.bbadis.2014.08.002

183 Basser, P. Fiber-tractography via diffusion tensor MRI (DT-MRI). (1998).

184 Mori, S., Crain, B. J. & van Zijl, P. C. M. 3D Brain Fiber Reconstruction from Diffusion MRI. *NeuroImage* **7**, S710 (1998). https://doi.org/https://doi.org/10.1016/S1053-8119(18)31543-X

185 Jeurissen, B., Descoteaux, M., Mori, S. & Leemans, A. Diffusion MRI fiber tractography of the brain. *NMR Biomed* **32**, e3785 (2019). https://doi.org/10.1002/nbm.3785

186 Basser, P. J., Pajevic, S., Pierpaoli, C., Duda, J. & Aldroubi, A. In vivo fiber tractography using DT-MRI data. *Magnetic Resonance in Medicine* **44**, 625-632 (2000). https://doi.org/10.1002/1522-2594(200010)44:4<625::Aid-mrm17>3.0.Co;2-o

187 Jeurissen, B., Leemans, A., Jones, D. K., Tournier, J. D. & Sijbers, J. Probabilistic fiber tracking using the residual bootstrap with constrained spherical deconvolution. *Hum Brain Mapp* **32**, 461-479 (2011). https://doi.org/10.1002/hbm.21032

188 Jeurissen, B., Leemans, A., Tournier, J. D., Jones, D. K. & Sijbers, J. Investigating the prevalence of complex fiber configurations in white matter tissue with diffusion magnetic resonance imaging. *Hum Brain Mapp* **34**, 2747-2766 (2013). https://doi.org/10.1002/hbm.22099

189 Dhollander, T., Raffelt, D., Mito, R. & Connelly, A. Improved white matter response function estimation for 3-tissue constrained spherical deconvolution. *Conference Paper* (2019).

190 Jeurissen, B., Tournier, J. D., Dhollander, T., Connelly, A. & Sijbers, J. Multi-tissue constrained spherical deconvolution for improved analysis of multi-shell diffusion MRI data. *Neuroimage* **103**, 411-426 (2014). https://doi.org/10.1016/j.neuroimage.2014.07.061

191 Dhollander, T., Raffelt, D. & Connelly, A. *Unsupervised 3-tissue response function estimation from single-shell or multi-shell diffusion MR data without a co-registered T1 image*. (2016).

192 Ullmann, J. F., Calamante, F., Collin, S. P., Reutens, D. C. & Kurniawan, N. D. Enhanced characterization of the zebrafish brain as revealed by super-resolution track-density imaging. *Brain Struct Funct* **220**, 457-468 (2015). https://doi.org/10.1007/s00429-013-0667-7

193 Pal, M. M. Glutamate: The Master Neurotransmitter and Its Implications in Chronic Stress and Mood Disorders. *Front Hum Neurosci* **15**, 722323 (2021). https://doi.org/10.3389/fnhum.2021.722323

194 Kim, Y. S. & Yoon, B. E. Altered GABAergic Signaling in Brain Disease at Various Stages of Life. *Exp Neurobiol* **26**, 122-131 (2017). https://doi.org/10.5607/en.2017.26.3.122

195 Kalra, S. & Arnold, D. L. Magnetic Resonance Spectroscopy for Monitoring Neuronal Integrity in Amyotrophic Lateral Sclerosis. *Advances in experimental medicine and biology* **576** (2006). https://doi.org/https://doi.org/10.1007/0-387-30172-0

196 Bertran-Cobo, C. *et al.* A Neurometabolic Pattern of Elevated Myo-Inositol in Children Who Are HIV-Exposed and Uninfected: A South African Birth Cohort Study. *Front Immunol* **13**, 800273 (2022). https://doi.org/10.3389/fimmu.2022.800273

197 Haase, A. *et al.* MR imaging using stimulated echoes (STEAM). *Radiology* **160**, 787-790 (1986). https://doi.org/10.1148/radiology.160.3.3737918

198 Ordidge, R. J., Connelly, A. & Lohman, J. A. B. Image-selected in Vivo spectroscopy (ISIS). A new technique for spatially selective nmr spectroscopy. *Journal of Magnetic Resonance (1969)* **66**, 283-294 (1986). https://doi.org/https://doi.org/10.1016/0022-2364(86)90031-4

199 Garwood, M. & DelaBarre, L. The Return of the Frequency Sweep: Designing Adiabatic Pulses for Contemporary NMR. *Journal of Magnetic Resonance* **153**, 155-177 (2001). https://doi.org/https://doi.org/10.1006/jmre.2001.2340

200 Bottomley, P. A. 4480228 Selective volume method for performing localized NMR spectroscopy. (1985).

201 Krug, J. R. *et al.* Assessing spatial resolution, acquisition time and signal-to-noise ratio for commercial microimaging systems at 14.1, 17.6 and 22.3 T. *J Magn Reson* **316**, 106770 (2020). https://doi.org/10.1016/j.jmr.2020.106770

202 Gruetter, R. *et al.* Resolution Improvements inin Vivo1H NMR Spectra with Increased Magnetic Field Strength. *Journal of Magnetic Resonance* **135**, 260-264 (1998). https://doi.org/https://doi.org/10.1006/jmre.1998.1542

203 Hoult, D. I. & Richards, R. E. The signal-to-noise ratio of the nuclear magnetic resonance experiment. *Journal of Magnetic Resonance* **213**, 329-343 (2011). https://doi.org/https://doi.org/10.1016/j.jmr.2011.09.018

204 Takahashi, M., Uematsu, H. & Hatabu, H. MR imaging at high magnetic fields. *European Journal of Radiology* **46**, 45-52 (2003). https://doi.org/https://doi.org/10.1016/S0720-048X(02)00331-5

205 Krupa, K. & Bekiesińska-Figatowska, M. Artifacts in magnetic resonance imaging. *Pol J Radiol* **80**, 93-106 (2015). https://doi.org/10.12659/pjr.892628

206 Zaitsev, M., Maclaren, J. & Herbst, M. Motion artifacts in MRI: A complex problem with many partial solutions. *Journal of Magnetic Resonance Imaging* **42**, 887-901 (2015). https://doi.org/https://doi.org/10.1002/jmri.24850

207 Soila, K. P., Viamonte, M. & Starewicz, P. M. Chemical shift misregistraton effect in magnetic resonance imaging. *Radiology* **153** (1984).

208 Lufkin, R., Anselmo, M., Crues, J. & Smoker, W. Magnetic field strength dependence of chemical shift artifacts. *Computerized Medical Imaging and Graphics* **12**, 8 (1988). https://doi.org/https://doi.org/10.1016/0895-6111(88)90002-X

209 Pusey, E., Yoon, C., Anselmo, M. L. & Lufkin, R. B. Aliasing artifacts in mr imaging. *Computerized Medical Imaging and Graphics* **12**, 219-224 (1988). https://doi.org/https://doi.org/10.1016/0895-6111(86)90003-0

210 Czervionke, L., Czervionke, J., Daniels, D. & Haughton, V. Characteristic features of MR truncation artifacts. *American Journal of Roentgenology* **151**, 1219-1228 (1988). https://doi.org/10.2214/ajr.151.6.1219

211 Farahani, K., Sinha, U., Sinha, S., Chiu, L. C. L. & Lufkin, R. B. Effect of field strength on susceptibility artifacts in magnetic resonance imaging. *Computerized Medical Imaging and Graphics* **14**, 409-413 (1990). https://doi.org/https://doi.org/10.1016/0895-6111(90)90040-I

212 Ullmann, J. F. P., Cowin, G., Kurniawan, N. D. & Collin, S. P. Magnetic resonance histology of the adult zebrafish brain: optimization of fixation and gadolinium contrast enhancement. *NMR in Biomedicine* **23**, 341-346 (2010). https://doi.org/https://doi.org/10.1002/nbm.1465

213 Ullmann, J. F. P., Cowin, G., Kurniawan, N. D. & Collin, S. P. A three-dimensional digital atlas of the zebrafish brain. *NeuroImage* **51**, 76-82 (2010). https://doi.org/https://doi.org/10.1016/j.neuroimage.2010.01.086

214 Hamilton, N., Allen, C. & Reynolds, S. Longitudinal MRI brain studies in live adult zebrafish. *NMR Biomed* **36**, e4891 (2023). https://doi.org/10.1002/nbm.4891

215 Cosgrove, K. P., Mazure, C. M. & Staley, J. K. Evolving Knowledge of Sex Differences in Brain Structure, Function, and Chemistry. *Biological Psychiatry* **62**, 847-855 (2007). https://doi.org/https://doi.org/10.1016/j.biopsych.2007.03.001

216 Hartmann, P., Ramseier, A., Gudat, F., Mihatsch, M. J. & Polasek, W. [Normal weight of the brain in adults in relation to age, sex, body height and weight]. *Pathologe* **15**, 165-170 (1994). https://doi.org/10.1007/s002920050040

217 Azevedo, F. A. *et al.* Equal numbers of neuronal and nonneuronal cells make the human brain an isometrically scaled-up primate brain. *J Comp Neurol* **513**, 532-541 (2009). https://doi.org/10.1002/cne.21974

218 Herndon, J. G., Tigges, J., Klumpp, S. A. & Anderson, D. C. Brain Weight Does Not Decrease with Age in Adult Rhesus Monkeys. *Neurobiology of Aging* **19**, 267-272 (1998). https://doi.org/https://doi.org/10.1016/S0197-4580(98)00054-2

219 Scott, J. A. *et al.* Longitudinal analysis of the developing rhesus monkey brain using magnetic resonance imaging: birth to adulthood. *Brain Struct Funct* **221**, 2847-2871 (2016). https://doi.org/10.1007/s00429-015-1076-x

220 Herculano-Houzel, S., Collins, C. E., Wong, P. & Kaas, J. H. Cellular scaling rules for primate brains. *Proceedings of the National Academy of Sciences* **104**, 3562-3567 (2007). https://doi.org/doi:10.1073/pnas.0611396104

221 Herculano-Houzel, S. & Lent, R. Isotropic fractionator: a simple, rapid method for the quantification of total cell and neuron numbers in the brain. *J Neurosci* **25**, 2518-2521 (2005). https://doi.org/10.1523/jneurosci.4526-04.2005

222 Kovačević, N. *et al.* A three-dimensional MRI atlas of the mouse brain with estimates of the average and variability. *Cerebral cortex* **15**, 639-645 (2005).

223 Welniak–Kaminska, M. *et al.* Volumes of brain structures in captive wild-type and laboratory rats: 7T magnetic resonance in vivo automatic atlas-based study. *PloS one* **14**, e0215348 (2019).

224 Herculano-Houzel, S., Mota, B. & Lent, R. Cellular scaling rules for rodent brains. *Proceedings of the National Academy of Sciences* **103**, 12138-12143 (2006). https://doi.org/doi:10.1073/pnas.0604911103

225 Friedrich, R. W., Genoud, C. & Wanner, A. A. Analyzing the structure and function of neuronal circuits in zebrafish. *Front Neural Circuits* **7**, 71 (2013). https://doi.org/10.3389/fncir.2013.00071

226 Hoult, D. I. & Richards, R. E. The signal-to-noise ratio of the nuclear magnetic resonance experiment. *Journal of Magnetic Resonance (1969)* **24**, 71-85 (1976). https://doi.org/https://doi.org/10.1016/0022-2364(76)90233-X